Monthly Notices of the ROYAL ASTRONOMICAL SOCIETY

MNRAS **512,** 328–347 (2022) https://doi.org/10.1093/mnras/stac399
Advance Access publication 2022 February 15

Radiation hydrodynamics modelling of kilonovae with SNEC

Zhenyu Wu [1]★ Giacomo Ricigliano [2] Rahul Kashyap,[3,4] Albino Perego[2,5] and David Radice[3,4,6]

[1]*School of Astronomy and Space Science, Nanjing University, Nanjing 210023, China*
[2]*Dipartimento di Fisica, Università di Trento, Via Sommarive 14, I-38123 Trento, Italy*
[3]*Institute for Gravitation and the Cosmos, The Pennsylvania State University, University Park, PA 16802, USA*
[4]*Department of Physics, The Pennsylvania State University, University Park, PA 16802, USA*
[5]*INFN-TIFPA, Trento Institute for Fundamental Physics and Applications, ViaSommarive 14, I-38123 Trento, Italy*
[6]*Department of Astronomy & Astrophysics, The Pennsyvlania State University, University Park, PA 16802, USA*

Accepted 2022 February 8. Received 2022 January 10; in original form 2021 November 17

ABSTRACT

We develop a method to compute synthetic kilonova light curves that combine numerical relativity simulations of neutron star mergers and the SNEC radiation–hydrodynamics code. We describe our implementation of initial and boundary conditions, r-process heating, and opacities for kilonova simulations. We validate our approach by carefully checking that energy conservation is satisfied and by comparing the SNEC results with those of two semi-analytic light-curve models. We apply our code to the calculation of colour light curves for three binaries having different mass ratios (equal and unequal mass) and different merger outcome (short-lived and long-lived remnants). We study the sensitivity of our results to hydrodynamic effects, nuclear physics uncertainties in the heating rates, and duration of the merger simulations. We find that hydrodynamics effects are typically negligible and that homologous expansion is a good approximation in most cases. However, pressure forces can amplify the impact of uncertainties in the radioactive heating rates. We also study the impact of shocks possibly launched into the outflows by a relativistic jet. None of our models match AT2017gfo, the kilonova in GW170817. This points to possible deficiencies in our merger simulations and kilonova models that neglect non-LTE effects and possible additional energy injection from the merger remnant and to the need to go beyond the assumption of spherical symmetry adopted in this work.

Key words: hydrodynamics – radiative transfer – methods: numerical – neutron star mergers.

1 INTRODUCTION

The orbit of compact binary neutron-star neutron-star (NSNS) and neutron-star black hole (NSBH) systems decays due to the emission of gravitational waves. Eventually, the two components of these binaries collide and merge. This process produces abundant gravitational radiation that can be detected by ground-based observatories such as LIGO, Virgo, and KAGRA (Abbott et al. 2020a). Tidal torques and shocks during these mergers can eject neutron rich material, the so-called dynamical ejecta (Ruffert, Janka & Schaefer 1996; Rosswog et al. 1999; Rosswog & Davies 2002; Rosswog & Liebendoerfer 2003; Rosswog, Ramirez-Ruiz & Davies 2003; Oechslin, Janka & Marek 2007; Sekiguchi et al. 2011; Bauswein, Goriely & Janka 2013; Rosswog, Piran & Nakar 2013; Sekiguchi et al. 2015; Foucart et al. 2016; Lehner et al. 2016; Radice et al. 2016; Sekiguchi et al. 2016; Bovard et al. 2017; Radice et al. 2018; Shibata & Hotokezaka 2019; Foucart et al. 2020; Nedora et al. 2020; Perego et al. 2020; Radice, Bernuzzi & Perego 2020; Vincent et al. 2020; Kullmann et al. 2021; Nedora et al. 2021b). Additional outflows are driven from the merger remnant by neutrino heating, magnetic, and other hydrodynamic effects on a time-scale of a few seconds, the so-called secular ejecta (Metzger, Piro & Quataert 2008, 2009; Dessart et al. 2009; Lee, Ramirez-Ruiz & López-Cámara 2009; Fernández & Metzger 2013; Metzger & Fernández 2014; Perego et al. 2014; Siegel, Ciolfi & Rezzolla 2014; Just et al. 2015; Martin et al. 2015; Fujibayashi et al. 2018; Metzger, Thompson & Quataert 2018; Siegel & Metzger 2018; Fernández et al. 2019; Nedora et al. 2019; Ciolfi & Kalinani 2020; De & Siegel 2020; Fujibayashi et al. 2020; Miller et al. 2020; Mösta et al. 2020; Just et al. 2021a; Metzger & Fernandez 2021; Shibata, Fujibayashi & Sekiguchi 2021). As this material decompresses, it undergoes r-process nucleosynthesis producing heavy elements (see e.g. Cowan et al. 2021; Perego, Thielemann & Cescutti 2021, for recent reviews). The nuclear decays of the unstable isotopes synthesized by the r-process heat the material and produce an electromagnetic transient known as kilonova (Li & Paczynski 1998; Kulkarni 2005; Metzger et al. 2010; Kasen, Badnell & Barnes 2013; Tanaka & Hotokezaka 2013; Metzger 2020; Hotokezaka et al. 2021).

This scenario has been confirmed by the multimessenger observations of GW170817 (Abbott et al. 2017; Arcavi et al. 2017; Chornock et al. 2017; Coulter et al. 2017; Cowperthwaite et al. 2017; Drout et al. 2017; Evans et al. 2017; Hallinan et al. 2017; Kasliwal et al. 2017; Murguia-Berthier et al. 2017; Nicholl et al. 2017; Smartt et al. 2017; Soares-Santos et al. 2017; Tanaka et al. 2017; Tanvir et al. 2017; Troja et al. 2017; Villar et al. 2017; Kasliwal et al. 2018; Rosswog et al. 2018; Waxman et al. 2018; Waxman, Ofek & Kushnir 2019; Margutti & Chornock 2020). Possible other kilonova detections have been reported in conjunction with some short gamma-ray burst, also thought to be the result of compact binary mergers (Nakar 2007; Berger 2014). These include a possible

★ E-mail: Zhenyu.Wu@ed.ac.uk

kilonova associated with GRB 130603B, the first claimed detection of a kilonova, and several other sources (Berger, Fong & Chornock 2013; Hotokezaka et al. 2013; Jin et al. 2013; Tanvir et al. 2013; Fong et al. 2014; Yang et al. 2015; Jin et al. 2016, 2020; Lamb et al. 2019; Troja et al. 2019; Rossi et al. 2020). Kilonovae appear to be commonly produced in NS mergers. However, observations also suggest that there might be significant variability between different events, possibly associated with a diversity in the outcome of NSNS and NSBH mergers (Kawaguchi, Shibata & Tanaka 2019) and in the viewing angle (Heinzel et al. 2021; Korobkin et al. 2021). Possibly due to the uncertain sky localization and larger distances, no kilonova counterpart has been reported for the second binary NS merger observed by LIGO and Virgo, GW190425 (Abbott et al. 2020b), or for GW200105 and GW200115, the first two NSBH merger events detected by LIGO and Virgo (Abbott et al. 2021).

Kilonova emission is produced by an expanding cloud of radioactive ejecta. The dynamics is not unlike that of Type Ia (thermonuclear) supernovae. Indeed, analogous analytic arguments can be used to predict the basic features of the light curve in both cases (Arnett 1980; Li & Paczynski 1998; Kulkarni 2005; Metzger et al. 2010; Chatzopoulos, Wheeler & Vinko 2012; Kashyap, Raman & Ajith 2019). However, there are some important differences between kilonovae and Type Ia supernovae. The expansion velocities of the kilonova outflows can be much larger than those of the supernova ejecta (Hotokezaka et al. 2018; Radice et al. 2018; Dean, Fernández & Metzger 2021; Nedora et al. 2021a). The radioactive heating of the kilonova material is not dominated by the decay chain of ^{56}Ni as in supernovae, but it is the result of the individual decays of thousands of unstable nuclides, resulting in a characteristic power-law decay (Metzger et al. 2010; Roberts et al. 2011; Korobkin et al. 2012; Lippuner & Roberts 2015; Hotokezaka, Sari & Piran 2017). The thermalization efficiency is also very different among different decay channels (Barnes et al. 2016; Hotokezaka et al. 2016; Hotokezaka & Nakar 2019; Kasen & Barnes 2019). Finally, the opacity of r-process elements produced in NS mergers is much higher than that of the iron produced in Type Ia supernovae, particularly when lanthanides are produced (Barnes & Kasen 2013; Kasen et al. 2013; Tanaka & Hotokezaka 2013; Fontes et al. 2020; Tanaka et al. 2020).

The broad features of the colour light curves of kilonovae can be reproduced with simple, one-zone, semi-analytical models (Li & Paczynski 1998; Kulkarni 2005; Metzger et al. 2010; Villar et al. 2017; Waxman et al. 2018), using parametrized heating rates and effective grey opacities obtained with Monte Carlo calculations. One of them is that of Perego, Radice & Bernuzzi (2017), who developed a multidimensional semi-analytical framework that included multiple outflow components and geometry information from ab initio simulations. This model was later used by Breschi et al. (2021) to perform a joint electromagnetic, gravitational-wave parameter estimation for GW170817. More advanced models use moment-based (Just et al. 2021b) or multifrequency Monte Carlo radiative transfer calculations (Kasen et al. 2013; Tanaka & Hotokezaka 2013; Kawaguchi, Shibata & Tanaka 2018; Wollaeger et al. 2018; Bulla et al. 2021; Korobkin et al. 2021). Surrogate models that can interpolate detailed Monte Carlo calculations have also been proposed (Coughlin et al. 2018). However, most previous works have ignored the hydrodynamics of the ejecta and adopted the assumption of homologous expansion. A notable exception is the work of Rosswog et al. (2014) and Grossman et al. (2014), which performed long-term smoothed particle hydrodynamics (SPH) simulations of the expanding tidal tail ejected in an NS merger. However, those simulations were based on the output of Newtonian NS merger simulations and did not include the contribution from the secular ejecta, which is currently thought to be dominant (Siegel 2019). Later works combined hydrodynamics simulations of the early phase of the outflows and homologous expansion Monte Carlo radiative transfer calculations (Kawaguchi et al. 2021; Klion et al. 2021a,b). The studies of Ishizaki et al. (2021) performed long-termn simulations of the ejecta in an NS merger focusing on the impact of the radioactive heating on the fallback but did not model the radiative transfer and the light curve from such flows.

In this work, we implement appropriate radioactive heating rates and opacities into the publicly available radiation hydrodynamics code SNEC (SuperNova Explosion Code; Morozova et al. 2015) to perform self-consistent calculation of kilonova light curves starting from the output of ab initio numerical relativity NS merger simulations. This approach allows us to study hydrodynamic effects on kilonova signals that have so far been neglected in calculation employing more sophisticated radiative transfer approaches. SNEC also provides a test platform for the development of microphysics routines that we ultimately plan to include in multidimensional calculations. Here, we discuss the implementation details of our code and we validate it against semi-analytic light-curve models and by carefully monitoring energy conservation. We use SNEC to study kilonova signals from realistic ejecta profiles obtained from merger simulations and we study the importance of hydrodynamic effects and the sensitivity of our results to nuclear physics uncertainties and to the duration of the simulations. Finally, we study the impact of shocks launched by the GRB jet into the ejecta on the light curves.

The rest of this paper is organized as follows. In Section 2, we describe all of the modifications we have made to the SNEC code to simulate kilonovae. In Section 3, we validate the code by checking energy conservation and comparing the results with two alternative semi-analytic models. In Section 4, we introduce the general features of the light curves from three realistic profiles. Then, we study the effects of various factors, including hydrodynamics, uncertainties in heating rates, duration of binary neutron-star (BNS) merger simulations, and the presence of shocks. We summarize and conclude in Section 5.

2 METHODS

2.1 Brief overview of SNEC

SNEC, the SuperNova Explosion Code, is a spherically symmetric 1D Lagrangian radiation–hydrodynamics code, primarily used to simulate core-collapse supernova explosions and generate synthetic colour light curves (Morozova et al. 2015, 2016; Piro & Morozova 2016; Morozova, Piro & Valenti 2017, 2018; Morozova et al. 2020). The SNEC code mainly uses Paczynski equation of state (EOS) (Paczynski 1983; Weiss et al. 2004), which includes the contributions from ions, electrons, and radiation. To get the fractions of atoms in different ionization states, SNEC solves the Saha equations. The code uses matter opacities κ from existing tables of Rosseland mean opacities (Iglesias & Rogers 1996) as a function of composition, temperature, and density. SNEC accounts for the radioactive heating due to ^{56}Ni and ^{56}Co and implements a simplified treatment of the associated γ-ray emission and thermalization. More details on the code can be found on SNEC's website.[1]

Kilonovae are powered by the radioactive decay of r-process elements synthesized in the ejecta. We use some of the SNEC modules but modify others to model kilonova emission. The main differences between the original SNEC code and our kilonova code

[1] https://stellarcollapse.org/index.php/SNEC.html

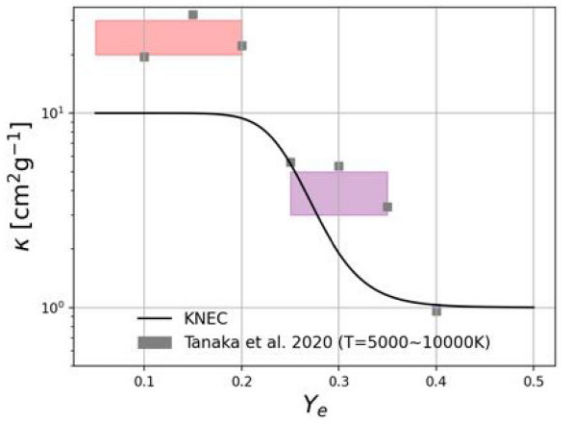

Figure 1. The solid line is opacity as a function of Y_e in our model (equation 1). The small grey squares show data from Tanaka et al. (2020), and the large rectangles are the suggested opacity ranges in their paper at 5000–10 000 K. Note that the opacities from Tanaka et al. (2020) decrease steeply at lower temperature. The opacities used in our calculations are somewhat smaller, since we take 10 cm^2 g^{-1} as their maximum value.

are the opacities (Section 2.2), heating rates (Section 2.3), and initial conditions (Section 2.4). Other differences are described in Section 2.5. Section 2.6 gives the formulae to calculate light curves in our model.

2.2 Opacities

Unlike supernovae, which are powered by iron group elements, r-process can generate heavier elements, including lanthanides and actinides. If present, lanthanides and actinides can increase the ejecta opacity by more than one order of magnitude to $\sim$10 cm^2 g^{-1}. The resulting strong optical line blanketing shifts the emission towards infrared bands (the so-called red kilonova, Roberts et al. 2011; Barnes & Kasen 2013; Kasen et al. 2013; Tanaka & Hotokezaka 2013). Whether or not these elements are produced by the r-process nucleosynthesis mainly depends on the electron fraction Y_e of the ejecta for the low entropy and fast expansion conditions expected in the ejecta from binary NS mergers. If $Y_e \lesssim 0.25$, then the ejecta will be lanthanide-rich. If $Y_e \gtrsim 0.25$, then r-process nucleosynthesis runs out of free neutrons before lanthanides can be produced (Hoffman, Woosley & Qian 1997; Lippuner & Roberts 2015).

In our model, we adopt grey opacity ranging from 1.0 cm^2 g^{-1} to 10.0 cm^2 g^{-1}, which we take to be a function of the initial Y_e. Our choice is motivated by the study of Tanaka et al. (2018), which showed that bolometric light curves computed assuming grey opacity in this range are in good agreement with those obtained with wavelength-dependent radiation transfer results. A similar range is adopted in Villar et al. (2017) to fit AT2017gfo, although their lower bound is smaller. We use the following formula to set the opacity:

$$\kappa = 1 + \frac{9}{1 + (4Y_e)^{12}} \quad [\mathrm{cm^2\,g^{-1}}]. \tag{1}$$

This smoothly transits from 1.0 cm^2 g^{-1} to 10.0 cm^2 g^{-1}. Accordingly, the opacity corresponding to $Y_e = 0.25$ is 5.5 cm^2 g^{-1}. This formula reproduces the expected rapid change in opacity at around $Y_e \simeq 0.25$. We explore the impact of the slope of the transition at $Y_e \simeq 0.25$ in Appendix A. There we show that the light curves are mostly insensitive to it.

Fig. 1 shows the comparison between our opacity model with the results of Tanaka et al. (2020). We remark that our model does not account for changes in the opacities, for example due to recombination, which are instead kept constant throughout our simulations. On the other hand, we emphasize that such treatment is consistent with the way these effective grey opacities have been constructed (Kasen et al. 2013; Tanaka & Hotokezaka 2013; Tanaka et al. 2020). To ease the comparison with previous works, we also restrict the maximum opacity to 10 cm^2 g^{-1} (Kasen et al. 2013; Tanaka & Hotokezaka 2013; Perego et al. 2017; Villar et al. 2017).

2.3 Heating rates

At the times relevant for kilonovae, the dominant source of heating is constituted by the decays of the heavy elements produced in the r-process nucleosynthesis. This energy release is described in terms of a heating rate, which can be computed by evolving the abundances of the numerous characteristic nuclides in time while accounting for their mutual interactions and decays. Nuclear heating simulations are highly dependent on the dynamical and thermodynamical conditions of the ejecta and, in particular, on the entropy, electron fraction, and expansion time-scale at the freeze-out from nuclear statistical equilibrium (NSE, see e.g. Hoffman et al. 1997; Lippuner & Roberts 2015). In addition, simulations also depend on the nuclear physics inputs: distinct theoretical nuclear mass models, reaction rates, or fission fragment distributions can lead to significantly different heating rates. This sensitivity is particularly strong at low electron fractions and the nuclear physics uncertainties can lead to changes in the predicted heating rates of about an order of magnitude (Rosswog et al. 2017; Zhu et al. 2021a).

Here, we consider the time-dependent heating rates resulting from the broad nucleosynthesis calculations reported in Perego et al. (2020). In that work, the nuclear abundance evolution of Lagrangian fluid elements was performed using the nuclear reaction network `SkyNet` (Lippuner & Roberts 2017) with the finite-range droplet macroscopic model (Möller et al. 2016) for the nuclear masses. Each `SkyNet` run was initialized from the electron fraction Y_e, entropy s, and expansion time-scale τ at a temperature of 6 GK in NSE conditions. More details about these nucleosynthesis calculations can be found in Perego et al. (2020). The heating rates used in this work were computed over a comprehensive grid of 11 700 distinct trajectories with $0.01 \leq Y_e \leq 0.48$ linearly spaced, $1.5\,k_B$ baryon^{-1} $\leq s \leq 200\,k_B$ baryon^{-1}, and 0.5 ms $\leq \tau \leq$ 200 ms log-spaced. These intervals are expected to bracket the properties of the ejecta from BNS and NSBH mergers. In the left-hand panel of Fig. 2, we report the heating rates obtained for the most representative conditions expected in the ejecta from NSNS mergers.

In order to derive the heating rate for arbitrary initial conditions, we construct fits to the trajectories obtained with `SkyNet`. The fits describe the heating rate over a time interval ranging from 0.1 s to 50 d after the merger. The fitting function distinguishes between two regimes. At early times, $t \lesssim 0.1$ d, we use the analytic fitting formula proposed by Korobkin et al. (2012), which was also derived from detailed nucleosynthesis calculations:

$$\dot{\epsilon}_r(t) = \epsilon_0 \left[\frac{1}{2} - \frac{1}{\pi}\arctan\left(\frac{t - t_0}{\sigma}\right)\right]^{\alpha}, \tag{2}$$

where ϵ_0, α, t_0, and σ are fitting parameters. At later times, $t \gtrsim 0.1$ d, we use a power-law fit, thus the fitting formula becomes:

$$\dot{\epsilon}_r(t) = \epsilon_0' t^{-\alpha'}, \tag{3}$$

where ϵ_0' and α' are additional fit parameters. The heating rate fits, as obtained from equations (2) and (3), are then joined together by a log-scaled smoothing procedure applied on the time interval 1×10^3

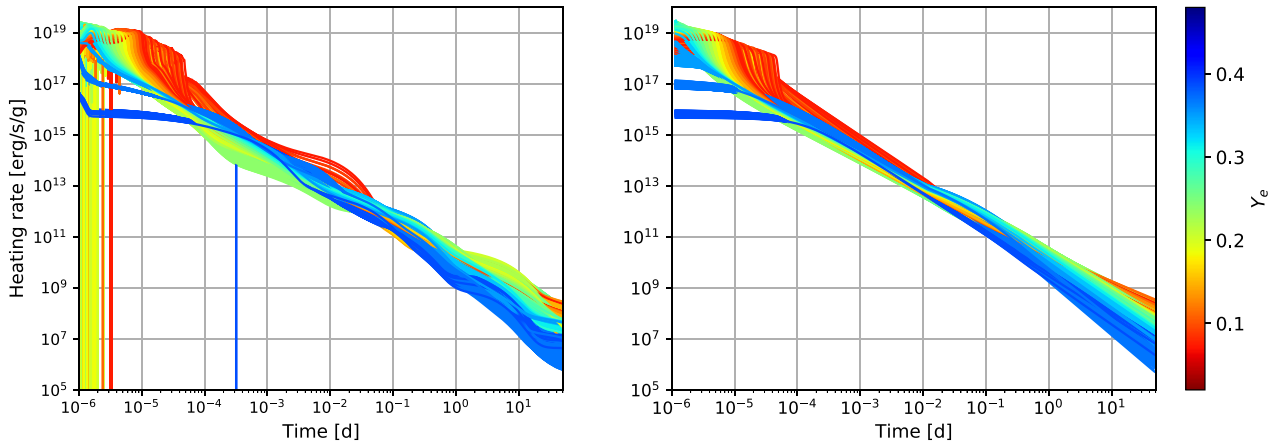

Figure 2. Heating rate trajectories for a grid of thermodynamic variables $0.05 \leq Y_e \leq 0.4$, $3\,k_B$/baryon $\leq s \leq 50\,k_B$/baryon, and 1 ms $\leq \tau \leq 30$ ms, corresponding (for visual clarity) to a subset of grid used in this work, as obtained by SkyNet (left) and as result of the fit discussed in the text (right). Trajectories are colour-coded according to the initial electron fractions. The vertical lines visible for some of the SkyNet trajectories correspond to sudden endoenergetic changes in the nuclear composition, possibly occurring during the r-process nucleosynthesis, which are averaged out in the fit procedure and do not significantly affect the heating rate at later times. The fitted heating rates agree well with the SkyNet calculations.

s $\leq t \leq 4 \times 10^4$ s, centred on $t \sim 0.1$ d in log-scale. The right-hand panel of Fig. 2 shows the fitted version of the heating rate trajectories presented in the left-hand panel.

The quality of a single fit is evaluated using a mean fractional log error as employed in Lippuner & Roberts (2015), defined as:

$$\Delta(\dot{\epsilon}_r) = \left\langle \frac{|\ln(\dot{\epsilon}_r^o(t)) - \ln(\dot{\epsilon}_r(t))|}{\ln(\dot{\epsilon}_r^o(t))} \right\rangle, \quad (4)$$

where $\dot{\epsilon}_r^o(t)$ is the original SkyNet heating rate trajectory, while the mean is performed over the entire time window 0.1 s $\leq t \leq 50$ d without weighing over the time-steps, in order to account for the original SkyNet resolution. For most trajectories, we find relative errors smaller than ∼1 per cent. The largest errors are found at the boundary of the SkyNet grid, where the relative error can be as large as ∼5 per cent.

The fitting coefficients are usually smooth functions of the thermodynamic variables, in particular, for $Y_e \leq 0.36$, $s \leq 90\,k_B$ baryon^{-1}, and $\tau \leq 30$ ms. Isolated points or boundary regions for which the continuity of the fitting coefficients was poor were removed from the fit. Since the regions where the parameters evolve smoothly are the most relevant for our calculations, we adopt a trilinear interpolation of the fitting coefficients as a function of Y_e, s, and τ. We validate this procedure by computing the error in the heating rate due to the fitting procedure for new SkyNet trajectories generated with input thermodynamic variables distinct from those used to construct the fit. The results for a subset of these trajectories are shown in Fig. 3. We find that the relative error of the fitting procedure is less than ∼1 per cent, well below the expected nuclear physics uncertainties.

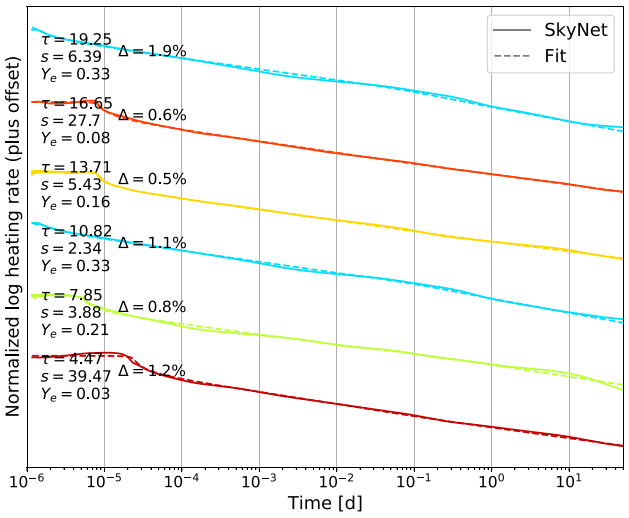

Figure 3. Comparison of the heating rates computed with SkyNet and with our fit for five different representative sets of off-grid thermodynamic variables. We also report the relative errors in the fits computed using equation (4). The typical errors in the heating rate due to the fitting procedure are of at most a few percent.

2.4 Initial and boundary conditions

We consider two kinds of ejecta profiles: (i) analytic wind profiles for code validation and parameter comparison, and (ii) realistic profiles extracted from NR simulations of merging neutron stars obtained with the WhiskyTHC code (Radice & Rezzolla 2012; Radice, Rezzolla & Galeazzi 2014a,b, 2015; Radice et al. 2016; Radice 2017; Radice et al. 2018). Both types of profile correspond to spherically symmetric outflows for which radius, temperature, density, velocity, initial Y_e, initial entropy, and expansion time-scale are given as a function of the enclosed mass. The initial entropy and expansion time-scale are new quantities that we have introduced and that are used to compute the heating rates and the opacities as discussed above. SNEC already tracks the electron fraction of the material; however, our calculations use only the initial Y_e of the matter. While this is consistent with our treatment of heating rates and opacity, which depends on the initial Y_e, this introduces an error at the level of the EOS, since we do not correctly account for the pressure contribution from free electrons. We leave the mean degree of ionization as a free parameter instead. As shown in Section 2.5, our tests indicate that this is a negligible effect, since matter is still dominated by the radiation pressure when homologous expansion sets in.

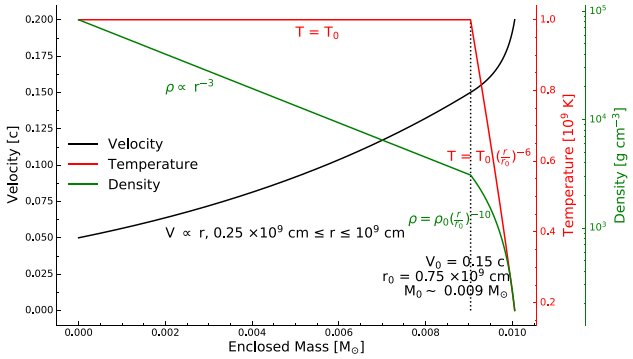

Figure 4. wind310T6 (optimal wind) profile: velocity, temperature, and density as a function of mass. The velocity is proportional to the radius. The maximum velocity and maximum radius are set to 0.2 c and 10^9 cm, respectively. The density decays with radius with a power-law exponent of 3, in the interior of the outflows, and of 10, in the outer regions, hence the name *wind310*. The turning point between the two power laws r_0 is 0.75×10^9 cm. The profile is designed with two power-law factors in order to fit homologous expansion. Outside $r = r_0$, the temperature drops with radius with a power-law factor of 6. This temperature drop reduces the otherwise large pressure gradients that would otherwise be present at the outer boundary producing very large expansion velocities.

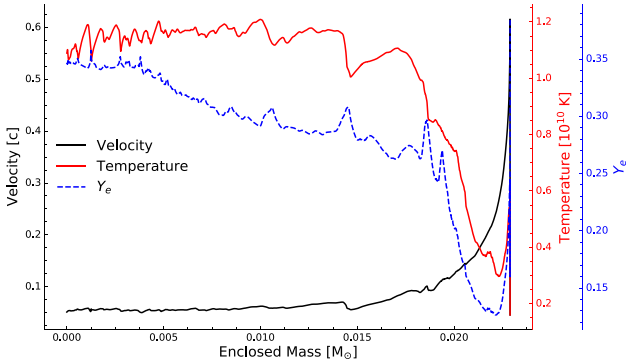

Figure 5. BLh profile: velocity, temperature, and Y_e as a function of mass. The profile is taken from `WhiskyTHC` simulation of binary NS merger (1.4 and 1.2 $M_\odot$, BLh EOS) at ∼0.11 s after merger. The velocity is almost constant but rises sharply to ∼0.6 c near the outer boundary. The low-Y_e component near the outer boundary is often referred to as 'lanthanide curtain'. However, there exists a high-Y_e component at the outermost tail of the ejecta.

We design analytic wind profiles similar to Metzger et al. (2010) and Tanaka & Hotokezaka (2013). The velocity is proportional to the radius and ranges between 0.05 c and 0.2 c. The maximum radius is set to 10^9 cm and the total mass is 0.01 $M_\odot$ by default. The initial electron fraction Y_e, entropy s, and expansion time-scale τ are uniform in the ejecta. We set s to 10 k_B baryon^{-1} and τ to 10 ms. In fact, the heating rates are relatively insensitive to s and τ. Inspired by Ishizaki et al. (2021), we use two power laws to describe the density as a function of r:

$$\begin{cases} \rho \propto r^{-k_1} & \text{for } r \le r_0, \\ \rho \propto r^{-k_2} & \text{for } r \ge r_0, \end{cases} \tag{5}$$

where k_1 is set to 3, and k_2 should be larger to represent a steep drop in density near the outer boundary. We experiment with various k_2 and find that $k_2 \gtrsim 10$ produces results for which there is good agreement between the full radiation–hydrodynamics calculations and calculations assuming homologous expansion (see Section 4.2). r_0 is set to 0.75×10^9 cm by default. We also use piecewise functions for the temperature T:

$$\begin{cases} T = T_0 = 10^9 K & \text{for } r \le r_0, \\ T \propto r^{-\alpha} & \text{for } r \ge r_0. \end{cases} \tag{6}$$

We find that the use of a power-law decay for T prevents the appearance of large pressure gradients at the outer boundary of our Lagrangean grid, which can otherwise generate unphysically large velocities for this type of artificial wind profiles. We find that $\alpha \gtrsim 6$ is enough to avoid this artefact. We denote the profile with ($k_1 = 3$, $k_2 = 10$, $\alpha = 6$) as *wind310T6* profile, or *optimal wind* profile (Fig. 4). More details regarding the boundary velocity problem with analytical wind profiles are discussed in Appendix B.

The NR profiles are constructed from outflow data recorded on fixed coordinate spheres as a function of time. In particular, we record the properties of matter crossing a sphere of radius $r \simeq 295$ km. We consider only matter that is unbound according to the Bernoulli criterion, that is with $hu_t < -1$, h being the enthalpy, and u_t the covariant time component of the fluid four velocity. Thermodynamic properties of the material, including Y_e, are then converted to spherical symmetry using a mass-weighted average and tabulated as a function of the enclosed ejecta mass, m. Since, the Y_e depends sensitively on the polar angle (Perego et al. 2017), this procedure introduces a systematic error in the computed light curves. We plan to address this in the future by performing isotropic-equivalent calculations that consider polar and equatorial ejecta separately. Since `SNEC` needs initial data at a fixed time and not inner boundary data as a function of time, we transform the data assuming homologous expansion. In particular, we compute $r(m)$ from the requirement that

$$m(r) = 4\pi \int_0^r \rho\, r^2\, \mathrm{d}r.$$

For this study, we consider the following three binaries.

(i) A 1.4 $M_\odot$–1.2 $M_\odot$ binary simulated with the BLh EOS (Bombaci & Logoteta 2018; Bernuzzi et al. 2020; Logoteta, Perego & Bombaci 2021) and evolved until 106 ms after merger. This binary produced a long-lived remnant. It is discussed in detail in Prakash et al. (2021).

(ii) A 1.364 $M_\odot$–1.364 $M_\odot$ binary targeted to GW170817 and simulated with the DD2 EOS (Hempel & Schaffner-Bielich 2010; Typel et al. 2010) until 113 ms after the merger. This binary produced a long-lived remnant. This system is discussed in detail in Nedora et al. (2019) and Nedora et al. (2021b).

(iii) A 1.4 $M_\odot$–1.2 $M_\odot$ binary simulated with the SFHo EOS (Steiner, Hempel & Fischer 2013) and evolved until 32 ms after the merger. This binary produced a short-lived remnant. It is discussed in detail in Radice et al. (2018).

All three simulations modelled neutrino emission and re-absorption using the M0 scheme of Radice et al. (2016). The DD2 binary also included a treatment of viscous angular momentum transport using the GRLES formalism (Radice 2017, 2020). We will refer to the three profiles generated from these simulations as being the DD2, SFHo, and BLh profiles, respectively.

Velocity, temperature, and initial Y_e for the BLh and DD2 profiles are shown in Figs 5 and 6. An important difference between these two models is that the BLh ejecta has an outer shell of low-Y_e material ($m \gtrsim 0.019$ $M_\odot$) ejected due to the tidal interaction between the two stars shortly prior to merger. This shell is absent for the equal mass DD2 model for which the outflows are driven by shocks and viscous and hydrodynamic torques on the post-merger disc. This

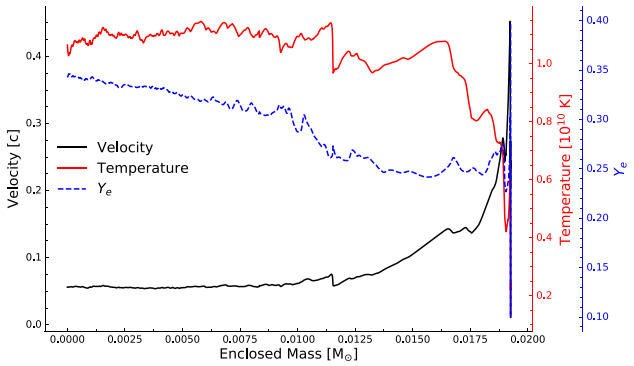

Figure 6. DD2 profile: velocity, temperature, and Y_e as a function of mass. The profile is taken from WhiskyTHC simulation of binary NS merger (1.36 and 1.36 solar mass, DD2 EOS) at ∼0.11 s. Most part of the DD2 profile has a Y_e larger than 0.25. This is due to lack of the low-Y_e tidal component, because the neutron stars are of equal mass here.

'lanthanide curtain' leads to very different behaviours between light curves of BLh and DD2 profiles (Section 4.1). Both profiles also include a fast expanding moderate Y_e outer shell of material. This mildly relativistic component of the outflow is accelerated by shocks after the merger, when the remnant bounces back (Radice et al. 2018; Nedora et al. 2021a). The SFHo profile is not shown, but it is qualitatively similar to the BLh profile. It also includes a lanthanide curtain. However, it has a smaller overall amount of ejecta, because black hole formation terminates the spiral wave-driven wind, which is the main mechanism driving the outflows in the first few tens of milliseconds after the merger (Nedora et al. 2021b). Additional outflow is expected on longer time-scales due to viscous and nuclear processes in the disc (Shibata & Hotokezaka 2019), but it is still not possible to simulate the binary over these longer time-scales in full 3D numerical relativity. Additionally, we have performed calculations in which we extrapolate the outflow rates from the simulation as a function of time, as discussed in Section 4.4 and Appendix C.

At the inner boundary, we keep the velocity constant, i.e. $v_1(t) = v_1(t = 0)$. Other boundary conditions are the same as in the original SNEC code. Luminosity is zero at the inner boundary ($L_1 = 0$). The artificial viscosity, density, specific internal energy, temperature, and pressure all vanish at the outer boundary, while the luminosity is extrapolated at first order ($Q_{\rm imax} = 0$, $\rho_{\rm imax+1/2} = 0$, $\epsilon_{\rm imax+1/2} = 0$, $T_{\rm imax+1/2} = 0$, $p_{\rm imax+1/2} = 0$, $L_{\rm imax} = L_{\rm imax-1}$).

2.5 Other differences from SNEC

2.5.1 Composition and EOS

The SNEC code computes the electron number density n_e and mean degree of ionization $\bar{y}$ by solving Saha equations. Due to the complexity of the ejecta compositions and the lack of detailed knowledge of ionization energies for r-process elements, we are not able to solve the Saha equations here. Instead, we take $\bar{y}$ to be a free parameter in our code. We also provide another free parameter, the mean molecular weight μ, such that $n_e = \frac{\bar{y}\rho}{m_p \mu}$, where m_p is the mass of the proton. In the calculations presented here, we fix the mean degree of ionization $\bar{y}$ to 2 and mean molecular weight μ is set to 100. In the calculation of the electron contribution to the pressure, we also fix the electron fraction to be 0.4. We remark that this electron fraction value is different from the initial Y_e used for the opacity and heating rates calculations. It roughly corresponds to the electron fraction of matter at the end of the nucleosynthesis. We have checked that our results are insensitive to these choices by performing test calculations with $\bar{y}$ varying between 1 and 50 and μ varying between 50 and 150.[2] We found that these parameters have a negligible impact on light curves. This is expected, since matter is radiation pressure dominated during the early phases of the expansion when pressure gradients drive the evolution of the outflows. Moreover, we neglect ionization correction terms in the specific internal energy and the partial derivative terms as shown below.

The ejecta EOS we use is basically the same as the Paczynski EOS in the original SNEC code, but the ionization correction terms are omitted. It is useful to go through the detailed calculations in the note on SNEC's website and compare them with our expressions shown below. In fact, SNEC's notes are based on Paczynski (1983) with the addition of corrections due to partial ionization (Weiss et al. 2004). The total pressure contains the contributions from ions, electrons, and radiation

$$p = P_{\rm ion} + P_e + P_{\rm rad}. \tag{7}$$

In the original SNEC codes, the specific internal energy ϵ is expressed as

$$\epsilon = \frac{3}{2} N k_B T + \frac{1}{f-1}\frac{P_e}{\rho} + \frac{aT^4}{\rho} + N\left\{\sum_k \nu_k \left[\sum_s y_s^k \left(\sum_{m=1}^{s} \chi_{m-1}^k\right)\right]\right\}, \tag{8}$$

where N is the number of ions per unit mass. ν_k is the number abundance of k-th element and y_s^k is the degree of s-th ionization of the k-th element. χ_{m-1}^k is the ionization energy for the ionization process $(m-1)$-th state $\rightarrow$ m-th state of k-th element. Since we do not have this information, we ignore the ionization correction term and use a simplified expression instead:

$$\epsilon = \frac{3}{2} N k_B T + \frac{1}{f-1}\frac{P_e}{\rho} + \frac{aT^4}{\rho}. \tag{9}$$

For the same reason, the partial derivative terms are simplified to:

$$\left(\frac{\partial \epsilon}{\partial T}\right)_\rho = \frac{3}{2} N k_B + \frac{4aT^3}{\rho} + \frac{1}{f-1}\frac{P_{\rm end}^2}{P_e \rho T} \tag{10}$$

$$\left(\frac{\partial p}{\partial T}\right)_\rho = N k_B \rho + \frac{4aT^3}{3} + \frac{P_{\rm end}^2}{P_e T} \tag{11}$$

$$\left(\frac{\partial p}{\partial \rho}\right)_T = N k_B T + \frac{1}{P_e}\left(\frac{P_{\rm end}^2}{\rho} + f\frac{P_{\rm ed}^2}{\rho}\right), \tag{12}$$

where $P_{\rm end}$ and $P_{\rm ed}$ denote the pressure of a non-degenerate and degenerate electron gas, respectively. The f in equations (8) to (12) is $f = \frac{d\ln P_{\rm ed}}{d\ln \rho} = \frac{5}{3}(\frac{P_{\rm ed}}{P_{\rm ednr}})^2 + \frac{4}{3}(\frac{P_{\rm ed}}{P_{\rm edr}})^2$, and $P_{\rm ednr}$ and $P_{\rm edr}$ correspond to the non-relativistic and relativistic cases for degenerate electron gas.

2.5.2 Explosion setup

SNEC provides two effective ways to explode the progenitor star of the supernova: thermal bomb and piston explosion. However, the designed analytic wind profiles and realistic profiles from WhiskyTHC already contain full initial conditions, so there is no need to set up explosions additionally. Thus, we simply set the explosion type to thermal bomb and set the energy input to 0. We use the thermal

[2]Changes in the post-nucleosynthesis Y_e are degenerate with $\bar{y}$ and μ.

bomb module only when we study the impact of shock cooling on kilonovae (see Section 4.5).

The SNEC code also implements a module called boxcar to smooth the compositional profile in the initial data. This tool mimics the mixing of ejecta during a supernova explosion. The boxcar has a given width, which is 0.4 $M_\odot$ by default. For each isotope, it sums up the isotope's mass within the width and distributes the total isotopic mass to each shell equally. The boxcar moves from the inner to the outer boundary, and then this procedure is repeated until smoothness is achieved. We do not use the boxcar in our calculations, because we do not expect large-scale mixing on the kilonova time-scale.

2.5.3 Central remnant

The mass of the inner remnant is also a parameter in the calculations as its gravitational pull can affect the evolution of the ejecta. We have fixed this inner remnant mass to be $M_{\rm remnant} = 3\ M_\odot$ in all calculations presented in this work.

2.6 Bolometric luminosities and multicolour luminosities

Blackbody radiation assumption for kilonovae was commonly used in previous research, such as the single-temperature model in Li & Paczynski (1998), and multicomponent models in Villar et al. (2017) and Perego et al. (2017). The spectra of AT2017gfo were close to blackbody in the first ∼2 d (Nicholl et al. 2017; Pian et al. 2017). Non-thermal radiation is negligible at $T \sim 5000\ K$, although it may become important at late times when the ejecta becomes transparent (Kasen et al. 2013; Tanaka & Hotokezaka 2013).

We compute the emergent radiation from the photosphere and from all the mass shells above it using a multitemperature blackbody model. In particular, we estimate the bolometric light curve as:

$$L_{\rm bol} = L_{\rm ph} + \int_{r_{\rm ph}}^{r_{\rm max}} \dot{\epsilon}\, {\rm d}m, \tag{13}$$

where $L_{\rm ph}$ is the luminosity at the photosphere, $r_{\rm ph}$ is the photospheric radius, $r_{\rm max}$ is the outer boundary in our simulation, and $\dot{\epsilon}$ is the effective heating rate per unit mass. $\dot{\epsilon} = \epsilon_{\rm th}\dot{\epsilon}_{\rm r}$, $\dot{\epsilon}_{\rm r}$ is the heating rate introduced in Section 2.3, and $\epsilon_{\rm th}$ is the thermalization efficiency, which is set to 0.5 by default.

The observed flux density at frequency ν is

$$f_\nu = \frac{1}{4\pi D^2}\left(\frac{\pi L_{\rm ph}}{\sigma T_{\rm ph}^4} B_\nu(T_{\rm ph}) + \int_{r_{\rm ph}}^{r_{\rm max}} \frac{\pi\dot{\epsilon}}{\sigma T^4} B_\nu(T)\, {\rm d}m\right), \tag{14}$$

where σ is the Stefan–Boltzmann constant, B_ν is the blackbody function, and D is the luminosity distance to the source. Throughout this work, we fix D to 40 Mpc, the approximate distance to AT2017gfo (Hjorth et al. 2017). Unlike the original SNEC code, we do not set a temperature floor here. We report our results using the AB magnitude system:

$$m_{\rm AB} = -2.5\log_{10}\left(\frac{\int f_\nu (h\nu)^{-1} e(\nu){\rm d}\nu}{\int 3631{\rm Jy}(h\nu)^{-1}e(\nu){\rm d}\nu}\right). \tag{15}$$

We compute light curves in different bands using filter functions $e(\nu)$ downloaded from the SVO Filter Profile Service[3] (Rodrigo, Solano & Bayo 2012; Rodrigo & Solano 2020). We primarily use CTIO and Gemini bands.

[3]http://svo2.cab.inta-csic.es/theory/fps/

3 CODE VALIDATION

3.1 Energy conservation

The equation of energy conservation for the whole system is:

$$\frac{\rm d}{{\rm d}t}\int_\Omega \rho\left(\epsilon + \frac{1}{2}|\boldsymbol{v}|^2\right){\rm d}V = \int_\Omega \rho \boldsymbol{f_b}\cdot\boldsymbol{v}\,{\rm d}V - \int_{\partial\Omega} p\boldsymbol{v}\cdot{\rm d}\boldsymbol{S} - \int_{\partial\Omega}\boldsymbol{f_s}\cdot{\rm d}\boldsymbol{S} + \dot{Q}, \tag{16}$$

where Ω is a material volume (a region moving with the fluid), ρ is the matter density, ϵ is the specific internal energy of the fluid (including the radiation), v is the fluid velocity, and p is the pressure. d/dt is the total time derivative. In our simulations, the surface force $\boldsymbol{f_s}$ is zero, while the body force $\boldsymbol{f_b}$ is the gravitational force. $\dot{Q} = H - L_{\rm bol}$ is the net cooling/heating due to nuclear decays H and emission $L_{\rm bol}$. This last term also includes the energy deposited into the outflows by the GRB jet, discussed in Section 4.5.

We can rewrite the energy conservation equation as:

$$\frac{d}{dt}(E_{\rm int} + E_{\rm kin} + E_{\rm grav}) = \dot{Q} - \int p\boldsymbol{v}\cdot d\boldsymbol{S}, \tag{17}$$

where

$$E_{\rm int} = 4\pi\int_{r_1}^{r_{\rm max}} \rho\,\epsilon\, r^2\,{\rm d}r, \tag{18}$$

$$E_{\rm kin} = \frac{4\pi}{2}\int_{r_1}^{r_{\rm max}} \rho v^2\, r^2\,{\rm d}r, \tag{19}$$

$$E_{\rm grav} = -4\pi\int_{r_1}^{r_{\rm max}} \rho\,\frac{G\mathcal{M}}{r}\, r^2\,{\rm d}r, \tag{20}$$

r_1 and $r_{\rm max}$ are the inner and outer radius of the ejecta and $\mathcal{M} = m(r) + M_{\rm remnant}$ is the enclosed mass including the central remnant. Since the outer boundary condition is $p_{\rm imax} = 0$, the $p{\rm d}V$ term includes only a contribution from the inner boundary:

$$-\int_{r_1}^{r_{\rm max}} p\boldsymbol{v}\cdot d\boldsymbol{S} = 4\pi\, p_1 v_1 r_1^2,$$

where p_1, v_1, and r_1 are pressure, radial velocity, and radius at the inner boundary, respectively. The gravitational energy $E_{\rm grav}$ is dominated by the contribution of the gravitational attraction to the central remnant.

To test how well energy is conserved in our calculations, we integrate equation (17) to obtain an overall energy balance. Here, we discuss energy conservation in the context of the optimal wind profile with initial $Y_{\rm e} = 0.1$, which is a representative case. In Fig. 7, E1 is the total energy of the ejecta including internal, kinetic, and gravitational energy. E2 is the initial total energy of the ejecta plus the net cumulative energy injected/released by r-process heating, $p{\rm d}V$ work at boundary and radiation emission. Eheating (t) ($= \int_0^t H\,{\rm d}t$) is the r-process heating, and Eradiation (t) ($= \int_0^t L_{\rm bol}{\rm d}t$) is the energy loss due to kilonova emission. If energy were perfectly conserved, then E1 and E2 would be identical. Since energy is not perfectly conserved in our simulation, we monitor |E1 − E2| to check the level of violation of energy conservation. That said, we find that SNEC conserves energy with a high degree of precision. In the case of the optimal wind profile, the maximum relative difference between E1 and E2 is ∼0.01 per cent. In the case of the BLh profile, the dynamics is more complex, but energy is also conserved to better than 1 per cent (see Appendix D).

Fig. 7 also shows the relative importance of the different forms of energy in the outflows. Overall, most of the energy is in the form of kinetic energy. Internal energy roughly balances gravity at very

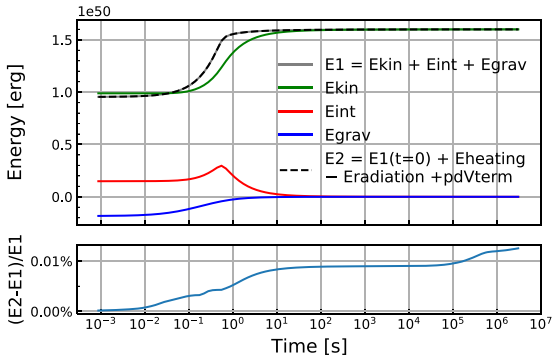

Figure 7. Energy conservation of the optimal wind with $Y_e = 0.1$. E1 is the total energy of the ejecta (gravitational + kinetic + internal) as a function of time. E2 is the initial total energy of the ejecta plus the net cumulative energy injected/released by r-process heating, pdV work at boundary, and radiation emission. Perfect energy conservation would imply E1 = E2. Their maximum relative difference here is around 0.01 per cent, indicating that our simulation well conserves energy.

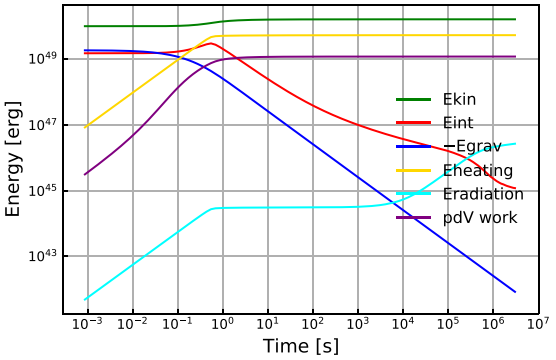

Figure 8. Energy budget for the optimal wind with $Y_e = 0.1$. The total energy budget is dominated by the kinetic energy. Only a small fraction of the energy is radiated. The internal energy and gravitational energy become less important as the ejecta cools and moves away from the central engine. The pdV term and the energy from heating are most important at around 1 s, when the bulk of the neutron captures is taking place in the r-process.

early times $t \lesssim 0.1$ s and peaks at a $t \lesssim 1$ s. At a time of about 1 s, r-process heating peaks and the internal energy now provides a significant contribution to the energy budget and can play a role in the dynamics of the outflows. This is consistent with the findings of Rosswog et al. (2014), who reported that the inclusion/omission of r-process heating leads to appreciable differences in the structure of the outflows after about 1 s. Foucart et al. (2021) also discuss the importance of heating in the context of neutron star binary merger simulations.

Fig. 8 shows the energy balance in logarithmic scale. We find that the heating and pdV work at inner boundary are important when r-process nucleosynthesis is taking place. Only a small fraction of the overall energy of the ejecta is radiated.

3.2 Comparison with analytic models

We compare the SNEC calculations with two alternative semi-analytic models: SADS (semi-analytic diffusion solver) and Arnett–Chatzopoulos–Villar's (ACV) single-component semi-analytic model. SADS implements a semi-analytic formula for the kilonova luminosity as proposed by Wollaeger et al. (2018). The model considers a homogeneous sphere with constant density, temperature, and opacity, which expands homologously starting from a few hours after merger. We model the radioactive heating in the ejecta using the heating rates described in Section 2.3. A semi-analytic solution of the radiative transfer equations is obtained under the assumption that matter is optically thick. The opacity is calculated starting from the input Y_e by means of equation (1). Along with the thermodynamical ejecta properties defining heating rates, that is Y_e, s, and τ, the model considers the ejecta mass M_{ej} and its maximum expansion velocity v_{max} as input variables, while it assumes a fixed value of $T_0 = 10^4$ K for the temperature of the homogeneous sphere at the starting time $t_0 = 10^4$ s.

ACV (Arnett 1982; Chatzopoulos et al. 2012; Villar et al. 2017) is based on an analytic solution originally proposed by Arnett (1982) for light curves of Type II supernovae with ^{56}Ni heating only and later generalized to any given heating function by Chatzopoulos et al. (2012). The model treats a radiation-dominated gas in spherical symmetry with a homologous expansion law. The luminosity is obtained starting from the first law of thermodynamics for the expanding envelope and by invoking the diffusion approximation. A constant grey opacity is employed, and the input energy generation rate is provided by the radioactive heating rate in order to adapt the energy source to kilonovae. Villar et al. (2017) have used three ejecta components to obtain excellent agreement with data from GW170817. Here, we return to one-component spherically symmetric ejecta. Both opacity and heating rate models are the same as those employed by SNEC and SADS.

For this comparison, SNEC is prepared using the initial and boundary conditions described in Section 2.4 and Section 2.5. In particular, we initialize the simulations using the analytic *wind310T6* profile, which, as discussed in Section 4.2, is found to provide a good agreement between SNEC calculations performed in full radiation–hydrodynamics and those that instead assume homologous expansion.

Fig. 9 shows bolometric luminosity, AB magnitudes in a few different Gemini bands, photospheric radius, and effective photospheric temperature obtained from SNEC, SADS, and ACV models. All calculations assumed fiducial values of $M_{ej} = 0.01\,M_\odot$, $v_{max} = 0.2$ c, $Y_e = 0.1$, $s = 10\,k_B$ baryon^{-1}, and $\tau = 10$ ms. We emphasize that all three calculations have adopted the same heating rates, effective grey opacities, and heating efficiencies. The three models show good overall agreement in their prediction for the bolometric luminosity, especially on a time-scale of a few days from the merger. The agreement is somewhat worse at early and late times. SADS model tends to overestimate the luminosity at early times, since it assumes that all radioactive decay energy is immediately radiated as blackbody emission. ACV underestimates the bolometric luminosity and overestimates the photospheric radius at late times. This is due to the fact that in this model, the photospheric radius is assumed to coincide with the average ejecta radius $r_{avg} = v_{avg}t$, which increases indefinitely and eventually becomes unphysical. In addition, ACV does not account for any luminosity contribution from the optically thin region outside the photosphere. ACV can avoid the unphysical photospheric radius expansion by applying a temperature floor, as done by Villar et al. (2017) when comparing the three-component model with data from GW170817. On the other hand, ACV shows a better agreement with SNEC than SADS in the colour light curves, especially in the blue and optical bands. SADS prediction of a bluer spectrum is caused by its systematic overestimation of the effective photospheric temperature. This effect arises both because the bolometric luminosity is typically overestimated and because the

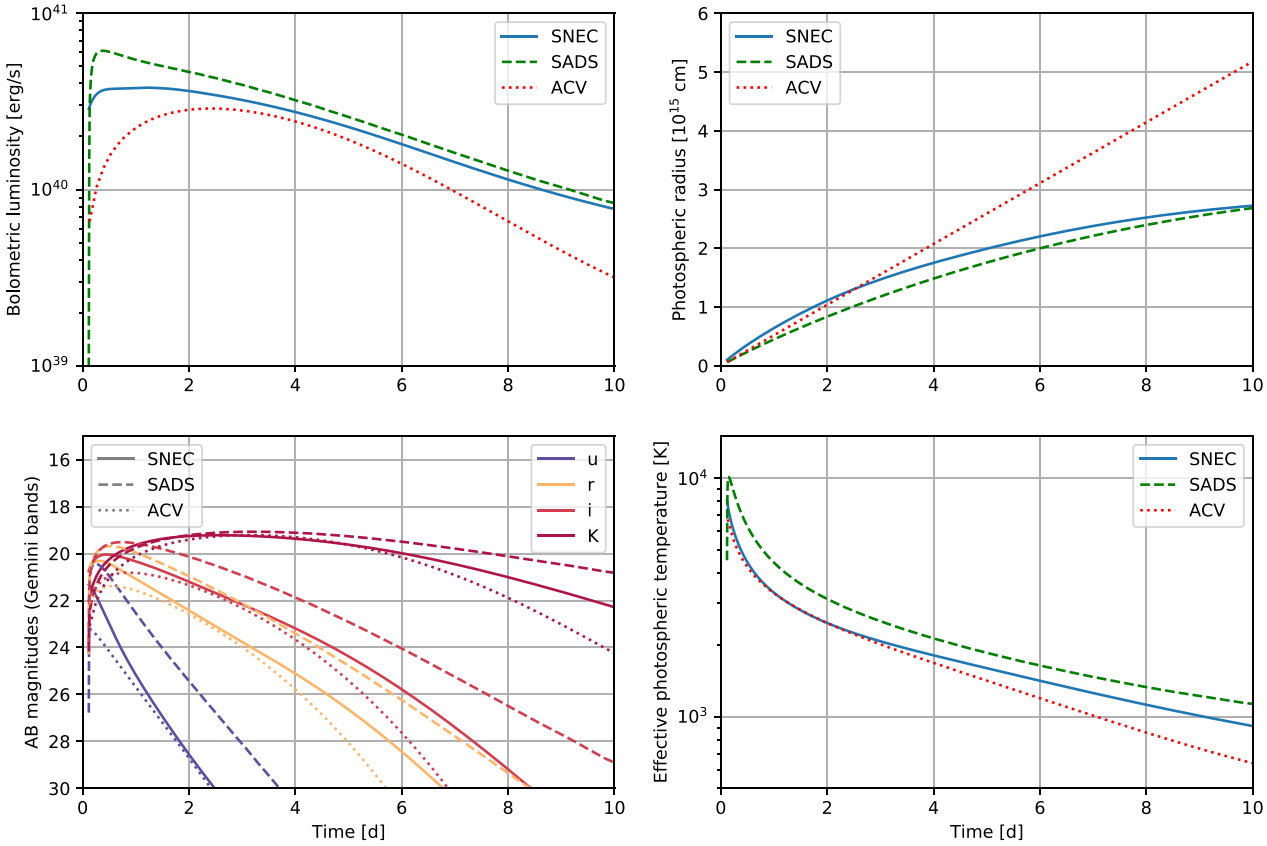

Figure 9. SNEC results for the bolometric luminosity and AB magnitudes using the optimal wind profile in correspondence of the input quantities $M_{\rm ej} = 0.01\,M_\odot$, $v_{\rm max} = 0.2$ c, $Y_{\rm e} = 0.1$, $s = 10\,{\rm k_B}$/baryon, and $\tau = 10$ ms, compared to the same results obtained with SADS and ACV models. Photospheric radius and effective temperature are shown for illustration.

photospheric radius, which is computed independently, is slightly underestimated. In SADS, the latter is found analytically by imposing a homologous density profile (Wollaeger et al. 2018) in the condition $\tau(r_{\rm ph}) = 2/3$, where $\tau(r)$ is the optical depth of the material at a certain radius r. This solution typically includes a first increase of the radius up to a maximum value, after which the latter decreases again back to zero. All models agree well in the infrared bands at a time-scale of a few days. This is not too surprising since hydrodynamic effects (Section 4.2) and the details of the radiative transfer in the ejecta become less important at these times.

Fig. 10 shows a comparison between SNEC and SADS for different values of the ejecta $Y_{\rm e}$. We find that for most values of $Y_{\rm e}$ SADS overestimates the bolometric luminosity, as it was the case in the previous comparison for $Y_{\rm e} = 0.1$. However, for large values of $Y_{\rm e} \gtrsim 0.4$, the situation is reversed and SADS underestimates the bolometric luminosity. The reason is that, for such values of $Y_{\rm e}$, the heating rate is dominated by the decay of a relatively small number of nuclear species, so it peaks at earlier times and then exponentially decays. This early energy release is not captured by SADS, since the SADS calculations start only ∼3 h after merger. On the other hand, the SNEC simulations also track the emission and thermalization of this energy and its subsequent release at later times.

Fig. 10 also shows some general trends in the light curve of kilonovae. In particular, it can be seen that the maximum bolometric luminosities for the optimal wind profiles with $M_{\rm ej} = 0.01 M_\odot$ and initial $v_{\rm max} = 0.2$ c range between 10^{40} and 10^{42} erg s^{-1}. Kilonova light curves produced by wind profiles with $Y_{\rm e} \gtrsim 0.25$ have larger

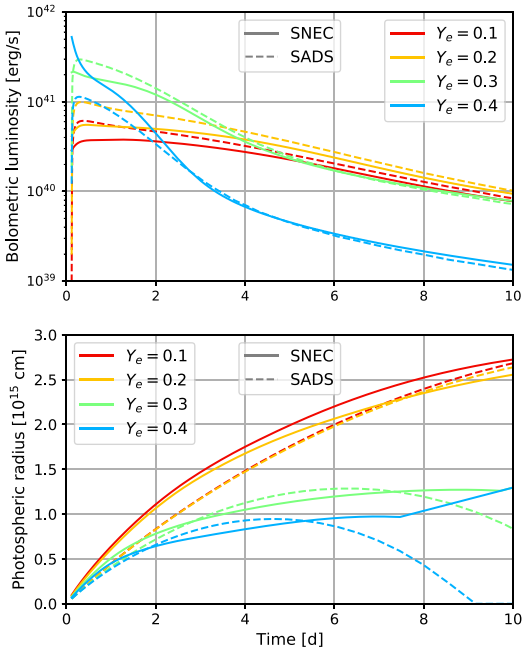

Figure 10. Bolometric luminosities and photospheric radii obtained with SNEC and SADS for different initial electron fractions at $M_{\rm ej} = 0.01\,M_\odot$, $v_{\rm max} = 0.2$ c, $s = 10\,{\rm k_B}$/baryon, and $\tau = 10$ ms.

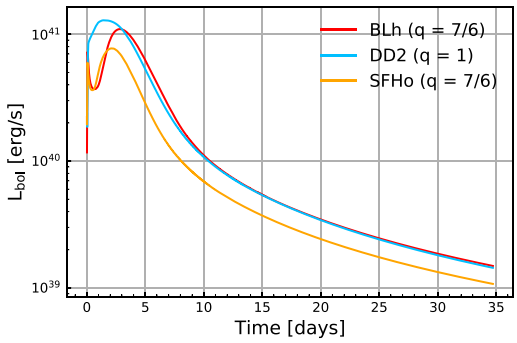

Figure 11. Bolometric light curves for the numerical relativity outflow profiles BLh, DD2, and SFHo (Section 2.4). The BLh and SFHo profiles have the same mass ratio $q = M_1/M_2 = 7/6$, and the DD2 profile is from an equal-mass neutron star binary. The BLh and DD2 outflows have a comparable mass and brightness after ∼3 d. The SFHo outflow is less massive and produces a dimmer kilonova. Both the BLh and SFHo kilonovae have double peaked light curves due to the lanthanide curtain effect, while the DD2 model does not.

peak luminosity and evolve more rapidly than those produced by more neutron-rich outflows. In fact, even if the total amount of heating produced by the r-process is larger for smaller Y_e, the overall radiated energy as well as its distribution in time depends on both the radioactive heating and the material opacity. Indeed, a small opacity is expected to cause the emission to peak earlier and the peak luminosity to be brighter. For a kilonova at a distance of 40 Mpc, the $Y_e = 0.1$ wind model with SNEC predicts a peak luminosity of about 21 magnitudes in the u band and of 19 magnitudes in the K_s band. The latter is reached at around 3 d after merger. The $Y_e = 0.4$ wind model with SNEC predicts a similar peak luminosity in the K_s band, but the peak is reached 1 d earlier. Moreover, the $Y_e = 0.4$ wind is much brighter in the u band and peaks at around 18.5 magnitudes. Ten days after the merger, the K_s-band magnitude has dropped to about 21 magnitudes for the $Y_e = 0.1$ wind and to about 27 magnitudes for the $Y_e = 0.4$ wind. These trends are consistent with the expectations (Metzger 2020).

4 FIRST APPLICATIONS OF SNEC

4.1 General features

We use SNEC to generate synthetic light curves using profiles from numerical relativity simulations of merging neutron stars. Fig. 11 shows the bolometric luminosities of the BLh, SFHo, and DD2 profiles. In the following discussion, we take these light curves as a baseline for comparison and as we study the impact of uncertainties in the heating rates, we consider time-extrapolated outflow rates from the simulations, and we study the impact of the thermal energy deposition due to a GRB jet and cocoon breaking through the ejecta. Among these outflow profiles, the SFHo profile has the smallest amount of ejecta ($\sim 9.2 \times 10^{-3}\ M_\odot$), because the associated merger simulation was discontinued after black hole formation, when the outflow rate due to the spiral-wave wind dropped to zero. Additional mass ejection would have been driven by viscous and nuclear processes in the disc over a time-scale of a few seconds, but these cannot yet be modelled in full 3D numerical relativity simulations. For these reasons, it is not surprising that the SFHo profile gives rise to the faintest kilonova among the considered models. The BLh and DD2 profiles have a similar amount of mass: $2.29 \times 10^{-2}\ M_\odot$ and $1.93 \times 10^{-2}\ M_\odot$, respectively. For this reason, they produce kilonovae that have very similar brightness after the first few days and both are brighter than the SFHo outflow. Interestingly, both the BLh and SFHo light curves have a double peak, while the DD2 light curve has a single peak. This is due to the presence of a low-Y_e component of the outflow for BLh and SFHo, which is absent in the DD2 profile (see Figs 5 and 6). This outflow component is due to the partial tidal disruption of the secondary star prior to merger. It is absent for the DD2 profile, which is associated to an equal mass merger.

These trends are reflected in Fig. 12, which shows the AB magnitudes of the kilonova emerging from these three profiles assuming a distance of 40 Mpc in different bands. The difference between the DD2 equal mass model and the others is even more apparent in the blue bands at early times. Our calculations suggest that high-cadence observations of kilonovae could constrain the presence/absence of a lanthanide curtain, which in turn would constrain the mass ratio of the binary. However, we caution the reader that the impact of the presence of a massive tidal tail on the light curve is likely exaggerated by the assumption of spherical symmetry used in our calculations. In reality, we expect that this effect will be prominent only for edge-on binaries.

Fig. 12 also shows the photometric data for AT2017gfo. The observation data are collected from kilonova.space[4] (Villar et al. 2017). The SNEC results use Gemini filters, and we also calculate CTIO bands, while the observation data are from various instruments. The differences in filters have little influence in the comparison. AT2017gfo is significantly brighter than any of our models. This is not unexpected, given the approximations in our models, most notably the fact that our merger simulations cannot yet self-consistently compute the full evolution of the post-merger disc due to the long time-scales involved and the assumption of spherical symmetry (Perego et al. 2014). In particular, the works of Perego et al. (2017), Korobkin et al. (2021), and Heinzel et al. (2021) showed that multidimensional effects and viewing angle, which we cannot take into account with SNEC, have a strong impact on the colour light curves from kilonovae. It is also worth mentioning that Breschi et al. (2021) performed a Bayesian selection analysis of the AT2017gfo and ruled out spherically symmetric kilonova models with high confidence. That said, fitting the observation is not the purpose of this paper, and we leave it to our future work.

The multicolour light-curve properties depend most directly on the initial Y_e at the luminosity shell of the ejecta. The latter is defined as the shell at which radiation diffusion and expansion time-scales become comparable, that is when the optical depth $\tau \sim c/v$. SNEC locates the luminosity shell by sweeping through the ejecta. It starts from the exterior, where $\tau = 0$, and moves towards the interior until τ becomes equal to c/v. At early times, the luminosity shell is close to the surface of the outflows, but at later times, the shell is found at increasingly large depth into the outflows, as the material expands and becomes transparent. Eventually, the luminosity shell becomes the inner boundary of the ejecta. Fig. 13 combines AB magnitudes in different bands for the BLh and DD2 profiles and the Y_e at the location of the luminosity shell, both as a function of time. Both profiles have an outer shell of rapidly expanding, high-Y_e material launched when the remnant bounces back after merger. In both cases, the kilonova is blue in the very first few hours after merger. The u-band magnitude for the BLh model reaches ∼20 magnitudes in the first hours of the merger, before dropping rapidly. In the BLh case, the

[4] https://kilonova.space

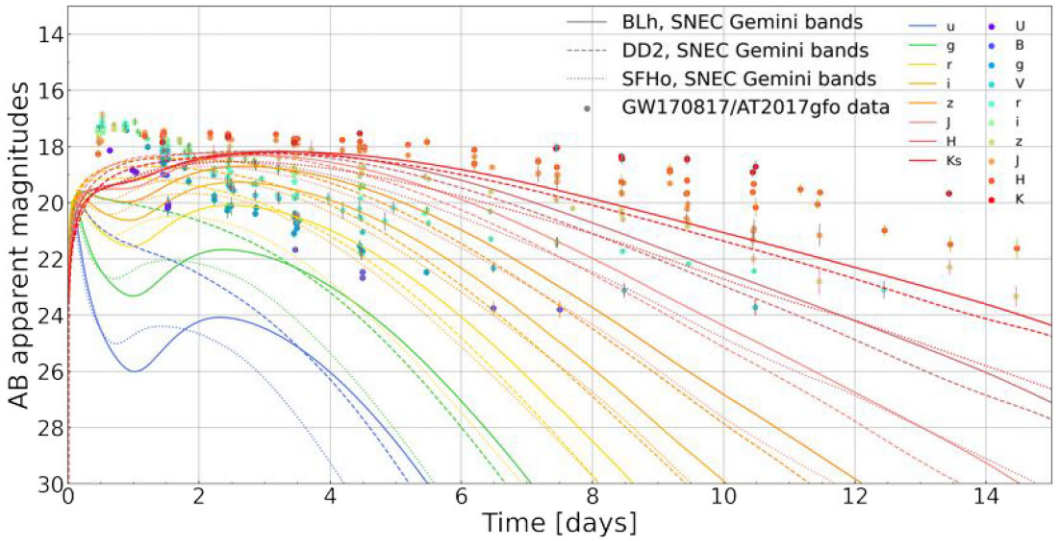

Figure 12. GW170817/AT2017gfo data (dots with error bars) and SNEC's AB apparent magnitudes of BLh (solid line), DD2 (dashed line), and SFHo (dotted line) at 40 Mpc. The observation data cover U to K bands for various telescopes. We adopt Gemini bands from u to K_s for SNEC results. This comparison shows that the current NR-informed models including BLh, DD2, and SFHo, which have an ejecta mass of 0.023 $M_\odot$, 0.019 $M_\odot$, and 0.009 $M_\odot$, do not match the observation. This indicates that a larger ejecta mass, or additional factors contributing to light curves, should be considered to fit the observation.

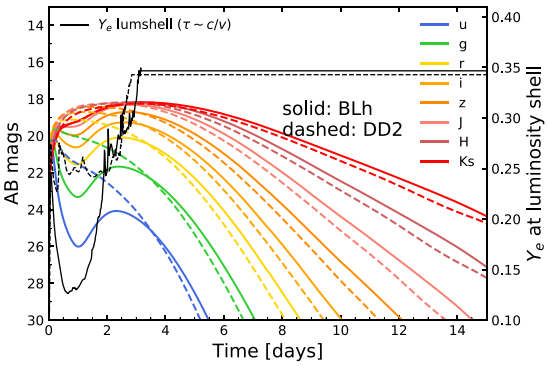

Figure 13. BLh and DD2 profile: AB apparent magnitudes and Y_e at luminosity shell. Luminosity shell locates at the point whose optical depth τ and velocity v satisfy $\tau = c/v$. When the ejecta becomes transparent enough, the luminosity shell falls on to the inner boundary. This figure shows that the first peak of BLh colour light curves is related to the outermost fast high-Y_e component of the ejecta. The gap between BLh's double peaks is due to the low-Y_e lanthanide curtain.

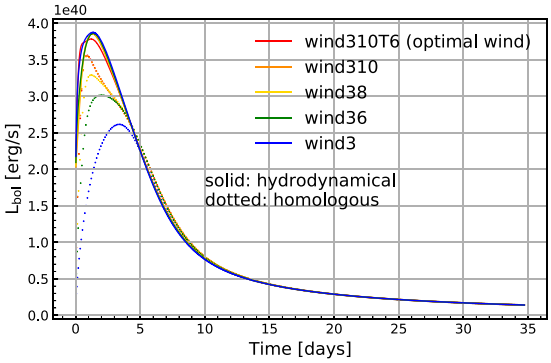

Figure 14. Bolometric light curves computed for different wind profiles assuming homologous expansion, or with full hydrodynamics. For all models, initial $Y_e = 0.1$, $s = 10$ k_B/baryon, and $\tau = 10$ ms. The solid lines show the hydrodynamical results from SNEC using the wind profiles. In general, the light curves coincide with each other. The dotted lines show homologous expansion results, i.e. hydrodynamics is turned off in SNEC. As we increase the second power-law index of density, the light curves get closer to hydrodynamical results.

kilonova becomes fainter and redder very quickly as the luminosity shell passes through the tidal tail, which is very neutron rich. The kilonova becomes bright again when the luminosity shell reaches the inner part of the ejecta, which has higher Y_e due to the combined effects of shock heating and neutrino irradiation from the central remnant (Radice et al. 2016).

4.2 Hydrodynamics

Most of the previous models, ranging from analytic and semi-analytic to Monte Carlo radiative transfer, assume homologous expansion and neglect the effects of pressure work (e.g. Tanaka & Hotokezaka 2013; Wollaeger et al. 2013; Bulla 2019). There are some attempts to combine hydrodynamics and radiative transfer (Gittings et al. 2008; Roth & Kasen 2015), but the study of the effects of hydrodynamics on kilonovae is very limited. Ishizaki et al. (2021) include hydrodynamics to study fallback accretion but does not include radiative transfer. Our work is one of the first radiation–hydrodynamics study of kilonovae. Radiation–hydrodynamics simulations are performed right after the merger until ∼35 d. The hydrodynamics can also be turned off in our code, so that the velocity is frozen and the ejecta undergoes free expansion ($v(t) = v(t = 0)$, $r = vt$).

Fig. 14 shows the bolometric light curves computed with and without the assumption of homologous expansions and for different wind profiles. The initial Y_e is set to 0.1 in all calculations. We remind the reader that wind3 profile refers to $\rho \propto r^{-3}$, while wind36, wind38, and wind310 use two power laws for density ($k_1 = 3$ and $k_2 = 6$, 8, 10, respectively). Their temperature is uniformly 10^9 K. Wind310T6 is the optimal wind profile introduced in Section 2.4. The

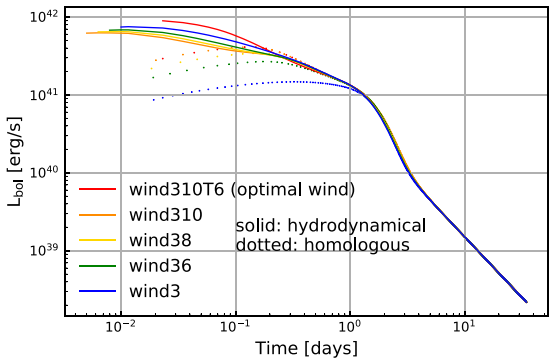

Figure 15. The same as Fig. 14 except $Y_e = 0.4$. After about 0.2 d, the hydrodynamical results for the optimal wind profile (wind310T6) agree with homologous expansion, while for other profiles, it takes longer time for the agreement.

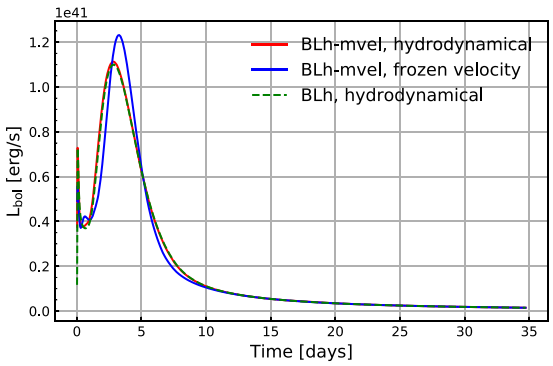

Figure 16. Effect of the hydrodynamics on the bolometric light curves for the BLh profile with modified velocity (BLh-mvel profile). The red line shows the results from the radiation–hydrodynamic calculations while the blue line shows the results obtained with hydrodynamics turned off and frozen velocity. As a comparison, the green dashed line shows the light curve for the original BLh profile. Hydrodynamic models predict faster expansion driven by pressure forces in the outflows and more rapidly evolving light curves.

bolometric luminosity from the hydrodynamic calculations (solid lines) is insensitive to the initial profiles, because the hydrodynamical evolution at the beginning of the simulation smooths the differences in the ejecta structures. On the other hand, the homologous expansion results vary by a factor of ∼2 depending on profiles. When increasing the second power-law factor for the density, we find better agreement between the homologous expansion results and those obtained with the hydrodynamics calculations. So, if the density profile includes a sharp drop near the outer boundary, which is reasonable as seen from NR simulations, homologous expansion is a good assumption. Fig. 15 shows the corresponding results for initial $Y_e = 0.4$. Also in this case, we find that homologous expansion calculations are very sensitive to the details of the outflow profiles. These tests suggest that wind profiles similar to the optimal wind profile introduced here should be employed for radiative transfer calculations that assume homologous expansion.

In addition to considering the impact of homologous expansion in the case of idealized wind profiles, we also consider its impact for the BLh profile, which we take as representative of a realistic profile from an NR simulation. Because there are fluctuations in the initial velocity distribution, we cannot directly turn off the hydrodynamics and freeze the velocity in this case. Indeed, the velocity v must increase monotonically with the radius r (or enclosed mass m) to avoid shell crossing. To achieve this, we replace the velocity in the BLh with a fit constructed using a monotonically increasing function (see Fig. B2 in Appendix B). We use this BLh-with-modified-velocity (BLh-mvel) profile for this test. The comparison of bolometric luminosity between BLh-mvel profile with and without hydrodynamics is shown in Fig. 16. In general, the two are consistent. The comparison between the multicolour light curves is shown in Fig. 17. We find that the inclusion of hydrodynamic effect shifts the second peak of the light curve by 1 d from ∼3 d after merger in the homologous expansion calculations to ∼2 d after merger in the radiation–hydrodynamics calculation. This difference is explained by the more rapid expansion of the lanthanide curtain driven by pressure forces in the hydrodynamics model. As a consequence of this fast expansion, the optical depth drops more rapidly and light from the lanthanide-poor inner part of the ejecta escapes at earlier times, so the kilonova peaks sooner. This effect can be seen in Fig. 17, where we also show the Y_e at the luminosity shell as a function of time. The faster expansion of the ejecta in the hydrodynamic models also leads to faster cooling for the hydrodynamics simulation compared to the

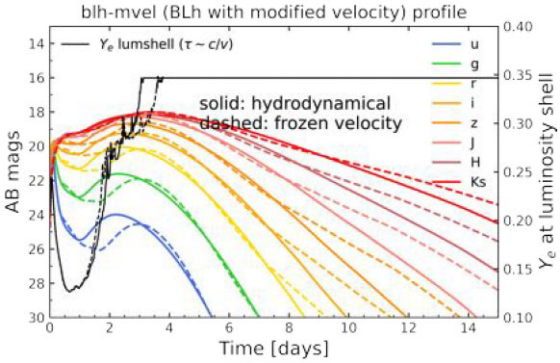

Figure 17. Effect of the hydrodynamics on the multicolour light curves for the BLh with modified velocity (BLh–mvel profile). The solid lines show the results from the radiation–hydrodynamic calculations, while dashed lines show the result obtained with hydrodynamics turned off and frozen velocity. The impact of hydrodynamics is particularly evident at early times in the blue bands.

homologous expansion simulation. This results in a more rapid drop in the colour light curves for the former after ∼9 d.

4.3 Impact of uncertainties in the heating rates

The energy released by nuclear decays and its thermalization efficiency are affected by systematic nuclear physics uncertainties (Barnes et al. 2021; Zhu et al. 2021b). These uncertainties span about an order of magnitude in the heating rate. To quantify their impact in our calculations, we perform simulations in which we vary the heating rates by a factor of 3 or 0.3. Fig. 18 shows the impact of changes in the heating rate in the case of the optimal wind profile with $Y_e = 0.1$. Unsurprisingly, the bolometric luminosity increases/decreases proportionally to the heating rate when we change the heating rates throughout the entire calculation. Interestingly, we find modest but measurable differences in the bolometric luminosity even if we change the heating rates only in the first 10 s of the calculations, that is during the time the actual r-process is actually

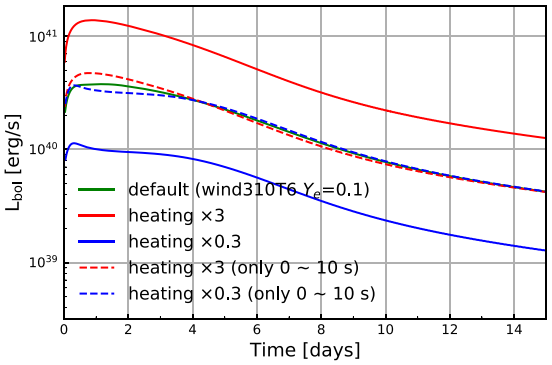

Figure 18. Bolometric light curves with different heating rates and the wind310T6 (optimal wind) profile with $Y_e = 0.1$, $s = 10$ k_B/baryon, and $\tau = 10$ ms. The green line represents the default heating rates introduced in Section 2.3, with thermalization efficiency $\epsilon_{th} = 0.5$. The red and blue solid lines display the light curves when the heating rate is multiplied by 3 and 0.3, respectively. The dashed light curves are obtained by changing the heating rates from the baseline only in the first 10 s.

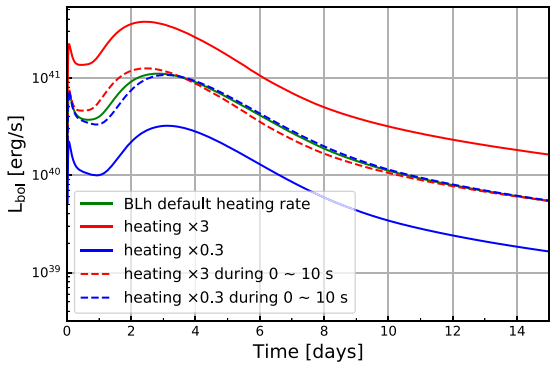

Figure 19. Bolometric light curves obtained with different heating rates and the BLh profile. The uncertainty of heating rates changes the light curves by an order of magnitude. The green line represents the default heating rates introduced in Section 2.3, with thermalization efficiency $\epsilon_{th} = 0.5$. The red and blue solid lines display the light curves when the heating rate is multiplied by 3 and 0.3, respectively. The dashed light curves are obtained by changing the heating rates from the baseline only in the first 10 s.

taking place. These differences persist for the first few days after merger.

The same trend is also seen in Fig. 19 for the BLh profile. In this case, the uncertainties in the heating rates in the first 10 s result in a shift of the peak time by about a day. The multicolour light curves corresponding to the models with baseline and increased heating rates are shown in Fig. 20. To investigate the origin of these differences, we have repeated the BLh calculation with the hydrodynamics turned off (assuming homologous expansion). We find that when the assumption of homologous expansion is used, the heating rate in the first 10 s has no impact on the light curve. We conclude that these changes in the light curve are the result of changes in the structure of the outflows. When the heating is increased in the first 10 s, this leads to higher temperatures and, consequently, higher pressures and, as a result, the expansion of the ejecta is slightly accelerated. The lanthanide curtain is lifted at earlier time and the light curve peaks sooner. These results are consistent with those of Klion et al. (2021a), who investigated the impact of r-process heating

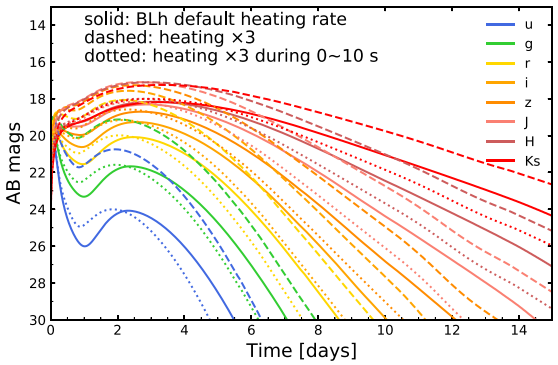

Figure 20. Multicolour light curves obtained with different heating rates and the BLh profile. The solid lines represent the Gemini band AB magnitudes predicted with the default heating rates. The dashed lines show the light curves with heating rates multiplied by 3. The dotted lines show the light curves obtained by multiplying the heating rates by 3 in the first 10 s only.

in the first 60 s of the outflows. They also find that enhanced heating at early times can produce slightly brighter light curves that peak at earlier times. However, in both our calculations and those of Klion et al. (2021a), these effects are modest and possibly degenerate with other properties of the ejecta.

4.4 Extrapolation of NR-informed models

The realistic profiles from our numerical relativity simulations capture only the amount of ejecta that has crossed a coordinate sphere with radius $r = 295$ km by the time we terminate our calculations. Here, we estimate the contribution of material ejected at later times by extrapolating the outflow rate in time. This is clearly a crude estimate, considering that the flow is expected to change in a qualitative way once the accretion rate on to the central object drops below a critical value (Beloborodov 2008; De & Siegel 2020). However, this approach let us test the sensitivity of our models to the length of the numerical relativity simulations without the need to introduce additional parameters.

We extrapolate the BLh outflow rate in time to 1.5, 2, and 10 times the total `WhiskyTHC` simulation duration, i.e. 0.167, 0.227, and 1.194 s after merger, respectively. The details of the extrapolation method are documented in Appendix C. Since the outflow rate is decaying, the overall ejecta mass increases only by a small factor, even when extrapolating to very late times (see Fig. C1). Consequently, the kilonova is only slightly brighter for the time-extrapolated profiles, as shown in Fig. 21. It should be noted that only the second peak of the BLh light curves is enhanced, which can be seen more clearly in multiband magnitudes (Fig. 22). This is expected, since during the first peak the luminosity shell is still localized at the outer surface of the ejecta, which is unaffected by the extrapolation. However, the kilonova becomes bluer at about 2 d, and the influence of lanthanide curtain on blue bands is weakened. This is also not surprising, since the material added to the profile by the extrapolation procedure has a high electron fraction, because the Y_e increases towards the interior of the ejecta (see Fig. 5).

4.5 Impact of shock cooling

Although the r-process heating can explain the general features of the GW170817/AT2017gfo kilonova, the nature of the emission in

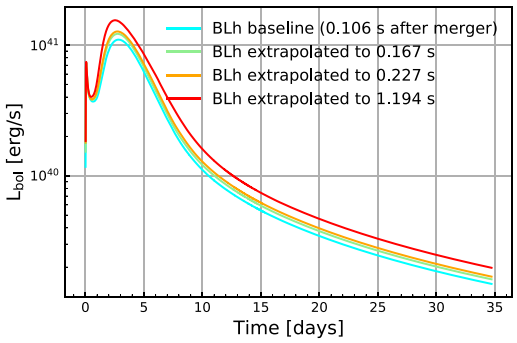

Figure 21. Bolometric light curves for the time-extrapolated BLh models. The original BLh profile, or BLh baseline, is extracted from WhiskyTHC simulation until 0.106 s after merger. We extrapolate the profile to 1.5, 2, and 10 times the total WhiskyTHC simulation time, which corresponds to 0.167, 0.227, and 1.194 s after merger, respectively.

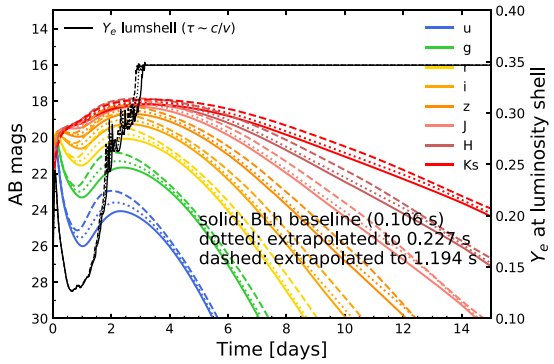

Figure 22. AB magnitudes and Y_e at the luminosity shell for the time-extrapolated BLh models. The late time ejecta predicted by the extrapolation procedure is not very neutron rich and contributes to only increase in the second peak of BLh multicolour light curves.

the first ∼1 d is still unclear. Piro & Kollmeier (2018) suggested that this early signal might be due to the radiative cooling of shock-heated material. The shock might have originated from the interaction between the GRB jet and the ejecta. When the jet propagates through the ejecta, it forms a hot cocoon around it and generates a shock structure including a reverse shock. The shock deposits energy as it propagates and heats the ejecta, although the way of energy deposition is not clear (Nakar & Piran 2017; Lazzati et al. 2017, 2021; Gottlieb, Nakar & Piran 2018a; Piro & Kollmeier 2018). According to (Duffell et al. 2018; Gottlieb et al. 2018a, b; Nativi et al. 2020; Lundman & Beloborodov 2021), the jet energy ranges between 10^{48} erg and 10^{51} erg, while the plausible cocoon energy is between 5×10^{45} erg and 5×10^{49} erg. The jet break out time was of 1.7 s in GW170817 (Abbott et al. 2017).

In this section, we use the BLh profile to explore the impact of shock cooling on kilonova emission. We use the 'thermal bomb' routine in SNEC to inject a shock with energy $E_{\rm shock}$ at the base of the ejecta. This routine injects energy with an exponential time dependency between the start time $t^{\rm b}_{\rm start}$ and the end time $t^{\rm b}_{\rm end}$ of the bomb:

$$P^{\rm b}(t) = d' e^{-c' t}, \tag{21}$$

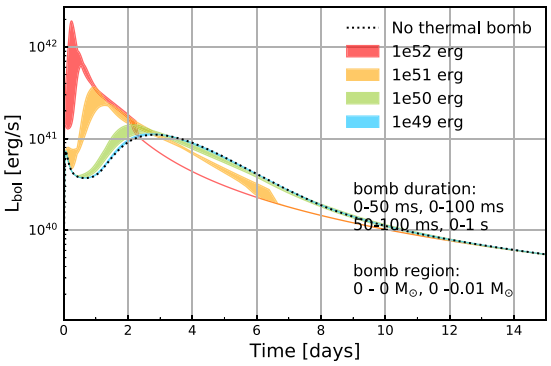

Figure 23. Bolometric light curve for the BLh profile with thermal bomb shock heating. The dotted line shows the baseline (no thermal bomb). The different colours represent different amounts of energy carried by the injected shock, ranging from 10^{49} erg to 10^{52} erg (isotropic equivalent). For each energy, the band spans results from different bomb configurations: time extent in {(0−50 ms), (0−100 ms), (50−100 ms), (0−1 s)}, spatial extent {(0, 0), (0−0.01$M_\odot$)}.

where $P^{\rm b}(t)$ is the injected bomb energy per unit time. The ratio $P^{\rm b}(t^{\rm b}_{\rm start})/P^{\rm b}(t^{\rm b}_{\rm end}) = R_t$ is set to 100 by default in SNEC. Therefore,

$$c' = \frac{\ln R_t}{\left(t^{\rm b}_{\rm end} - t^{\rm b}_{\rm start}\right)}, \quad d' = \frac{c' E_{\rm shock}}{e^{-c' t^{\rm b}_{\rm start}} - e^{-c' t^{\rm b}_{\rm end}}}. \tag{22}$$

Similarly, at each time, the energy is spread exponentially between the start point $m_{\rm start}$ and the end point $m_{\rm end}$:

$$P^{\rm b}_{{\rm m},i}(m_i) = b' e^{-a' m_i}. \tag{23}$$

The ratio $P^{\rm b}_{{\rm m},i}(m^{\rm b}_{\rm start})/P^{\rm b}_{{\rm m},i}(m^{\rm b}_{\rm end}) = R_m$ is also set to 100, then we obtain

$$a' = \frac{\ln R_m}{m^{\rm b}_{\rm end} - m^{\rm b}_{\rm start}}, \quad b' = \frac{d' e^{-c' t}}{\sum_i e^{-a' m_i} \Delta m_{i+1/2}}. \tag{24}$$

We test different configurations of these parameters and find that the results are not very sensitive to the time interval, which we vary between 0−50 ms, 0−100 ms, 50−100 ms, and 0−1 s, and to the choice of the spatial region in which the energy is injected, which we vary between 0−0 (i.e. deposited only at the inner boundary) and 0−0.01 $M_\odot$. The results are instead sensitive to the overall injected energy.

We find that shocks with $E_{\rm shock} < 10^{49}$ erg have negligible impact on the kilonova light curve. This is not too surprising, given that the initial kinetic energy in the ejecta is $\sim 10^{50}$ erg. However, it is important to remark that our calculations assume spherical symmetry, while the cocoon is expected to be asymmetric at the time of breakout. A very rough estimate of the impact of anisotropy can be obtained by using the isotropic equivalent energy of the shock, instead of its actual energy. In so doing, we effectively assume that the fluid elements are only weakly coupled in the angular direction. Accordingly, we interpret the SNEC calculations as describing the evolution of a portion of the outflow subtended by a fixed solid angle. A better treatment would require performing 2D axisymmetric or 3D simulations (Duffell et al. 2018; Gottlieb et al. 2018a, b; Nativi et al. 2020; Lundman & Beloborodov 2021).

We vary $E_{\rm shock}$ from 10^{49} erg to 10^{52} erg. Fig. 23 shows the bolometric light curves with shock injection. We find that, if the shock energy is large enough, it can increase the bolometric luminosity by up to an order of magnitude. The shock can also alter the morphology of the light curve, suppressing the minimum on the light curve at $t \simeq$

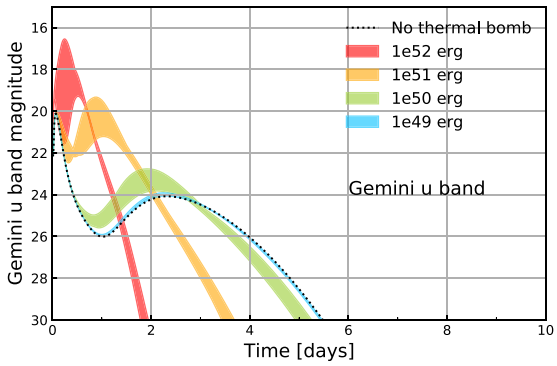

Figure 24. *u*-band light curve for BLh models with thermal bomb. A sufficiently strong shock can significantly accelerate the expansion of the ejecta. On the one hand, faster expansion and radiation from the shock cooling suppress the lanthanide curtain effect and boost the luminosity at early times. On the other hand, the fast expansion causes the material to become optically thin at early times, so the kilonova light curve evolves on shorter time-scales.

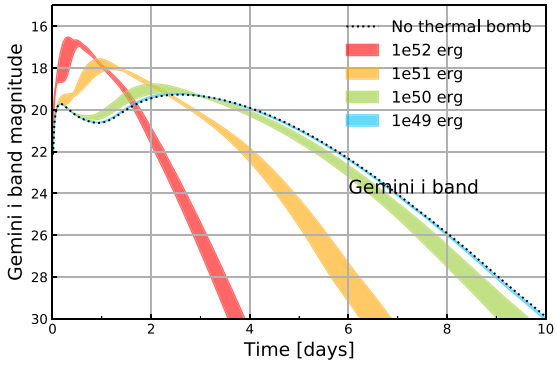

Figure 25. *i*-band light curve for BLh models with thermal bomb. This figure is to be contrasted with Fig. 24, which shows the *u*-band emission for the same models. The impact of a shock injected at the base of the outflow on the *i*-band light curve is similar, but somewhat less pronounced, than that on the *u*-band light curve.

1 d and thus hiding the lanthanide curtain. These changes are in part due to the radiative cooling of the shock heating material. However, the main effect of the shock is to accelerate the expansion of the ejecta which, as a result, becomes transparent at earlier times.

Figs 24–26 show the Gemini *u* band, *i* band, and K_s band of the results. The blue/optical bands are more significantly influenced by the shock, which can boost the luminosity of the kilonova by up to 4 magnitudes in these bands. The impact on the peak luminosity in the red/infrared bands is more modest, but we still find that an energetic shock can boost the luminosity by about 1 magnitude even in these bands. In all cases, we find that a shock at the base of the outflow can significantly accelerate the kilonova: making it peak at earlier times and fade more rapidly. Overall, our results motivate the need for further investigation of the impact of the jet on the kilonova emission using multidimensional models.

5 CONCLUSION AND DISCUSSION

We studied the kilonova emission from the ejecta of BNS mergers by means of radiation–hydrodynamical simulations. We considered both analytic wind profiles and ejecta profiles from numerical

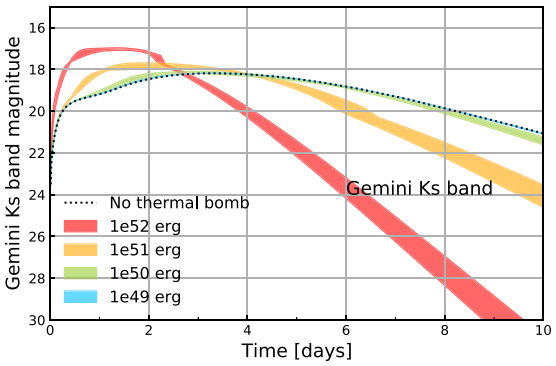

Figure 26. K_s-band light curve for BLh models with thermal bomb. This figure is to be contrasted with Figs 24 and 25, which show the *u*-band and *i*-band emissions for the same models. The more rapid expansion of the outflows caused by the shock also influences this band. With large thermal bomb energies, the kilonova is brighter and evolves on faster time-scales.

relativity simulations and then employed the SNEC code to compute the associated colour light curves. To this aim, we developed new modules for the SNEC code, including for the calculation of r-process heating rates and opacities, and specialized the built-in Paczynsky EOS in SNEC to the case of merger outflows. We validated our approach by carefully checking energy conservation and comparing our results with those obtained from simpler semi-analytic models. As first applications of the code, we computed self-consistent kilonova light curves from a set of merger simulations; we studied the impact of pressure forces and hydrodynamics, of nuclear physics uncertainties, and of shock cooling on the kilonova light curves.

We considered three merger simulations employing three EOS (BLh, DD2, and SFHo) and two different mass ratios. The DD2 binary considers an equal mass binary (1.365 $M_\odot$–1.365 $M_\odot$), while the BLh and SFHo consider binaries with a mass asymmetry (1.4 $M_\odot$–1.2 $M_\odot$). All the corresponding ejecta profiles show an outer fast component with high Y_e, but the bulk of the outflows has a moderate neutron richness. Additionally, the BLh and SFHo outflows have a very neutron-rich tidal component between the outer high Y_e outflow and the bulk of the outflow. The combined presence of a fast high-Y_e outer shell and of a lanthanide curtain results in a double-peaked morphology of the light curve. This is a new feature revealed by our calculations.

It is not our goal to fit observational data, but when comparing our models to AT2017gfo, we found them to be underluminous, especially in the first few days. This remains true even when considering outflow rates from the merger simulations extrapolated to late times. This may suggest that GW170817 ejected more mass than predicted by our models, or that the adopted heating rates and opacities are underestimated or overestimated, respectively. Shock cooling and, more in general, the interaction between the ejecta and the GRB jet might also alleviate this disagreement. That said our results should be considered as provisional, given our assumption of spherical symmetry in SNEC (Perego et al. 2017).

We studied the impact of hydrodynamic effects by comparing light curves produced with and without the assumption of homologous expansion. We found that hydrodynamics can have a substantial impact on the light curve, especially when considering idealized wind profiles. However, these effects are substantially smaller for more realistic wind profiles for which there are smaller pressure gradients close to the surface of the ejecta. The impact of hydrodynamics is also relatively small when considering ejecta from simulations.

We studied the impact of nuclear physics uncertainties on heating rates on the kilonova light curves. As expected, we find that the bolometric luminosities are directly proportional to the heating rate. Surprisingly, however, we also found that changes to the heating rate in the first 10 s can result in small but appreciable differences in the kilonova properties. These differences arise due to changes in the structure of the outflows resulting from the increased/decreased pressure.

Finally, we studied the impact of the interaction between the dynamical ejecta and the GRB jet. To this aim, we injected shocks at the base of the ejecta using the thermal bomb module of SNEC with different total energies and with different bomb parameters. We found that the shock has a substantial impact on the kilonova light curve when the energy of the shock is comparable to or larger than the initial kinetic energy of the ejecta ($\sim 10^{50}$ erg). The shock accelerates the ejecta which, as a result, becomes transparent at earlier times. The resulting kilonova light curves evolve more rapidly and are bluer. The shock injection impacts predominantly the UV/optical bands in the first $\sim$2 d of the merger.

The approach we have developed here is complementary to other efforts that employ wavelength-dependent Monte Carlo radiative transfer but neglect hydrodynamic effects. We have made a number of approximations that need to be improved to be able to compute reliable, realistic synthetic kilonova light curves from numerical relativity. Among these, the most serious one is the assumption of spherical symmetry. We plan to go beyond this approximation by porting the routines we have developed and tested with SNEC into the Athena++ code (Stone et al. 2020) and use a technique similar to that introduced by Habegger & Heitsch (2021) to track the expansion of the ejecta over a time-scale of several weeks. SNEC simulations could be post processed using Monte Carlo radiative transfer codes to compute improved colour light curve and to compute synthetic spectra. Other possible future avenue of research includes coupling SNEC with a nuclear reaction network like SkyNet and adopting time-dependent thermalization efficiencies and improved opacities.

ACKNOWLEDGEMENTS

We thank Viktoriya Morozova for help with the SNEC code. David Radice acknowledges funding from the U.S. Department of Energy, Office of Science, Division of Nuclear Physics under award number(s) DE-SC0021177 and from the National Science Foundation under grant nos. PHY-2011725, PHY-2020275, PHY-2116686, and AST-2108467.

DATA AVAILABILITY

Simulation data produced as part of this work will be made available upon request to the corresponding author.

REFERENCES

Abbott B. et al., 2017, Astrophys. J. Lett., 848, L12
Abbott B. et al., 2020a, Living Rev. Rel., 23, 3
Abbott B. et al., 2020b, Astrophys. J. Lett., 892, L3
Abbott R. et al., 2021, Astrophys. J. Lett., 915, L5
Arcavi I. et al., 2017, ApJ, 848, L33
Arnett W. D., 1980, ApJ, 237, 541
Arnett W. D., 1982, Astrophys. J., 253, 785
Barnes J., Kasen D., 2013, Astrophys.J., 775, 18
Barnes J., Kasen D., Wu M.-R., Martínez-Pinedo G., 2016, Astrophys.J., 829, 110
Barnes J., Zhu Y., Lund K., Sprouse T., Vassh N., McLaughlin G., Mumpower M., Surman R., 2021, Astrophys.J., 918, 44
Bauswein A., Goriely S., Janka H.-T., 2013, Astrophys.J., 773, 78
Beloborodov A. M., 2008, AIP Conf. Proc., 1054, 51
Berger E., 2014, Ann. Rev. Astron. Astrophys., 52, 43
Berger E., Fong W., Chornock R., 2013, Astrophys. J. Lett., 774, L23
Bernuzzi S. et al., 2020, Mon. Not. Roy. Astron. Soc., 497, 1488
Bombaci I., Logoteta D., 2018, Astron. Astrophys., 609, A128
Bovard L., Martin D., Guercilena F., Arcones A., Rezzolla L., Korobkin O., 2017, Phys. Rev. D, 96, 124005
Breschi M., Perego A., Bernuzzi S., Del Pozzo W., Nedora V., Radice D., Vescovi D., 2021, Mon. Not. Roy. Astron. Soc., 505, 1661
Bulla M. et al., 2021, Mon. Not. Roy. Astron. Soc., 501, 1891
Bulla M., 2019, MNRAS, 489, 5037
Chatzopoulos E., Wheeler J., Vinko J., 2012, Astrophys. J., 746, 121
Chornock R. et al., 2017, Astrophys. J. Lett., 848, L19
Ciolfi R., Kalinani J. V., 2020, Astrophys. J. Lett., 900, L35
Coughlin M. W. et al., 2018, Mon. Not. Roy. Astron. Soc., 480, 3871
Coulter D. et al., 2017, Science, 358, 1556
Cowan J. J., Sneden C., Lawler J. E., Aprahamian A., Wiescher M., Langanke K., Martínez-Pinedo G., Thielemann F.-K., 2021, Rev. Mod. Phys., 93, 015002
Cowperthwaite P. et al., 2017, Astrophys. J. Lett., 848, L17
De S., Siegel D., 2020, ApJ, 921, 94
Dean C., Fernández R., Metzger B. D., 2021, ApJ, 921, 161
Dessart L., Ott C., Burrows A., Rosswog S., Livne E., 2009, Astrophys. J., 690, 1681
Drout M. et al., 2017, Science, 358, 1570
Duffell P. C., Quataert E., Kasen D., Klion H., 2018, ApJ, 866, 3
Evans P. et al., 2017, Science, 358, 1565
Fernández R., Metzger B. D., 2013, Mon. Not. Roy. Astron. Soc., 435, 502
Fernández R., Tchekhovskoy A., Quataert E., Foucart F., Kasen D., 2019, Mon. Not. Roy. Astron. Soc., 482, 3373
Fong W. et al., 2014, Astrophys. J., 780, 118
Fontes C., Fryer C., Hungerford A., Wollaeger R., Korobkin O., 2020, Mon. Not. Roy. Astron. Soc., 493, 4143
Foucart F., O'Connor E., Roberts L., Kidder L. E., Pfeiffer H. P., Scheel M. A., 2016, Phys. Rev. D, 94, 123016
Foucart F., Duez M. D., Hebert F., Kidder L. E., Pfeiffer H. P., Scheel M. A., 2020, Astrophys. J. Lett., 902, L27
Foucart F., Moesta P., Ramirez T., Wright A. J., Darbha S., Kasen D., 2021, Phys. Rev. D, 104, 123010
Fujibayashi S., Kiuchi K., Nishimura N., Sekiguchi Y., Shibata M., 2018, Astrophys. J., 860, 64
Fujibayashi S., Wanajo S., Kiuchi K., Kyutoku K., Sekiguchi Y., Shibata M., 2020, Astrophys. J., 901, 122
Gittings M. et al., 2008, Comput. Sci. Discovery, 1, 015005
Gottlieb O., Nakar E., Piran T., 2018a, Mon. Not. Roy. Astron. Soc., 473, 576
Gottlieb O., Nakar E., Piran T., Hotokezaka K., 2018b, MNRAS, 479, 588
Grossman D., Korobkin O., Rosswog S., Piran T., 2014, Mon. Not. Roy. Astron. Soc., 439, 757
Habegger R., Heitsch F., 2021, ApJS, 256, 42
Hallinan G. et al., 2017, Science, 358, 1579
Heinzel J. et al., 2021, Mon. Not. Roy. Astron. Soc., 502, 3057
Hempel M., Schaffner-Bielich J., 2010, Nucl. Phys. A, 837, 210
Hjorth J. et al., 2017, Astrophys. J. Lett., 848, L31
Hoffman R. D., Woosley S. E., Qian Y. Z., 1997, ApJ, 482, 951
Hotokezaka K., Nakar E., 2019, ApJ, 891, 152
Hotokezaka K., Kyutoku K., Tanaka M., Kiuchi K., Sekiguchi Y., Shibata M., Wanajo S., 2013, Astrophys. J. Lett., 778, L16
Hotokezaka K., Wanajo S., Tanaka M., Bamba A., Terada Y., Piran T., 2016, Mon. Not. Roy. Astron. Soc., 459, 35
Hotokezaka K., Sari R., Piran T., 2017, Mon. Not. Roy. Astron. Soc., 468, 91
Hotokezaka K., Kiuchi K., Shibata M., Nakar E., Piran T., 2018, Astrophys. J., 867, 95
Hotokezaka K., Tanaka M., Kato D., Gaigalas G., 2021, MNRAS, 506, 5863
Iglesias C. A., Rogers F. J., 1996, Astrophys. J., 464, 943
Ishizaki W., Kiuchi K., Ioka K., Wanajo S., 2021, ApJ, 922, 185

Jin Z.-P. et al., 2016, Nature Commun., 7, 12898
Jin Z.-P., Xu D., Fan Y.-Z., Wu X.-F., Wei D.-M., 2013, Astrophys. J. Lett., 775, L19
Jin Z.-P., Covino S., Liao N.-H., Li X., D'Avanzo P., Fan Y.-Z., Wei D.-M., 2020, Nature Astron., 4, 77
Just O., Bauswein A., Pulpillo R. A., Goriely S., Janka H. T., 2015, Mon. Not. Roy. Astron. Soc., 448, 541
Just O., Goriely S., Janka H.-T., Nagataki S., Bauswein A., 2021a, MNRAS, 509, 1377
Just O., Kullmann I., Goriely S., Bauswein A., Janka H.-T., Collins C. E., 2021b, MNRAS, 510, 2820
Kasen D., Barnes J., 2019, Astrophys. J., 876, 128
Kasen D., Badnell N., Barnes J., 2013, Astrophys. J., 774, 25
Kashyap R., Raman G., Ajith P., 2019, Astrophys. J. Lett., 886, L19
Kasliwal M. et al., 2017, Science, 358, 1559
Kasliwal M. M. et al., 2018, MNRAS, 510, L7
Kastaun W., Galeazzi F., 2015, Phys. Rev. D, 91, 064027
Kawaguchi K., Shibata M., Tanaka M., 2018, Astrophys. J. Lett., 865, L21
Kawaguchi K., Shibata M., Tanaka M., 2019, ApJ, 889, 171
Kawaguchi K., Fujibayashi S., Shibata M., Tanaka M., Wanajo S., 2021, Astrophys. J., 913, 100
Klion H., Tchekhovskoy A., Kasen D., Kathirgamaraju A., Quataert E., Fernández R., 2021a, 510, 2968
Klion H., Duffell P. C., Kasen D., Quataert E., 2021b, Mon. Not. Roy. Astron. Soc., 502, 865
Korobkin O. et al., 2021, Astrophys. J., 910, 116
Korobkin O., Rosswog S., Arcones A., Winteler C., 2012, Mon. Not. Roy. Astron. Soc., 426, 1940
Kulkarni S., 2005, preprint (arXiv:astro-ph/0510256)
Kullmann I., Goriely S., Just O., Ardevol-Pulpillo R., Bauswein A., Janka H.-T., 2021, MNRAS, 510, 2804
Lamb G. et al., 2019, ApJ, 883, 48
Lazzati D., Deich A., Morsony B. J., Workman J. C., 2017, Mon. Not. Roy. Astron. Soc., 471, 1652
Lazzati D., Perna R., Ciolfi R., Giacomazzo B., López-Cámara D., Morsony B., 2021, ApJ L, 918, L6
Lee W. H., Ramirez-Ruiz E., López-Cámara D., 2009, ApJ, 699, L93
Lehner L., Liebling S. L., Palenzuela C., Caballero O., O'Connor E., Anderson M., Neilsen D., 2016, Class. Quant. Grav., 33, 184002
Li L.-X., Paczynski B., 1998, Astrophys. J. Lett., 507, L59
Lippuner J., Roberts L. F., 2015, Astrophys. J., 815, 82
Lippuner J., Roberts L. F., 2017, Astrophys. J. Suppl., 233, 18
Logoteta D., Perego A., Bombaci I., 2021, Astron. Astrophys., 646, A55
Lundman C., Beloborodov A. M., 2021, ApJ L, 907, L13
Mösta P., Radice D., Haas R., Schnetter E., Bernuzzi S., 2020, Astrophys. J. Lett., 901, L37
Margutti R., Chornock R., 2020, ARA&A, 59
Martin D., Perego A., Arcones A., Thielemann F.-K., Korobkin O., Rosswog S., 2015, Astrophys. J., 813, 2
Metzger B. et al., 2010, Mon. Not. Roy. Astron. Soc., 406, 2650
Metzger B. D., 2020, Living Rev. Rel., 23, 1
Metzger B. D., Fernández R., 2014, Mon. Not. Roy. Astron. Soc., 441, 3444
Metzger B. D., Fernandez R., 2021, Astrophys. J. Lett., 916, L3
Metzger B., Piro A., Quataert E., 2008, Mon. Not. Roy. Astron. Soc., 390, 781
Metzger B., Piro A., Quataert E., 2009, Mon. Not. Roy. Astron. Soc., 396, 304
Metzger B. D., Thompson T. A., Quataert E., 2018, Astrophys. J., 856, 101
Miller J. M., Sprouse T. M., Fryer C. L., Ryan B. R., Dolence J. C., Mumpower M. R., Surman R., 2020, Astrophys. J., 902, 66
Möller P., Sierk A. J., Ichikawa T., Sagawa H., 2016, Atom. Data Nucl. Data Tabl., 109-110, 1
Morozova V., Piro A., Renzo M., Ott C., Clausen D., Couch S., Ellis J., Roberts L., 2015, Astrophys. J., 814, 63
Morozova V., Piro A. L., Renzo M., Ott C. D., 2016, Astrophys. J., 829, 109
Morozova V., Piro A. L., Valenti S., 2017, Astrophys. J., 838, 28
Morozova V., Piro A. L., Valenti S., 2018, Astrophys. J., 858, 15
Morozova V., Piro A. L., Fuller J., Van Dyk S. D., 2020, Astrophys. J. Lett., 891, L32
Murguia-Berthier A. et al., 2017, ApJ L, 848, L34
Nakar E., 2007, Phys. Rept., 442, 166
Nakar E., Piran T., 2017, Astrophys. J., 834, 28
Nativi L., Bulla M., Rosswog S., Lundman C., Kowal G., Gizzi D., Lamb G. P., Perego A., 2020, Mon. Not. Roy. Astron. Soc., 500, 1772
Nedora V. et al., 2020, ApJ, 906, 98
Nedora V. et al., 2021b, Astrophys. J., 906, 98
Nedora V., Bernuzzi S., Radice D., Perego A., Endrizzi A., Ortiz N., 2019, Astrophys. J. Lett., 886, L30
Nedora V., Radice D., Bernuzzi S., Perego A., Daszuta B., Endrizzi A., Prakash A., Schianchi F., 2021a, MNRAS, 506, 5908
Nicholl M. et al., 2017, Astrophys. J. Lett., 848, L18
Oechslin R., Janka H.-T., Marek A., 2007, Astron. Astrophys., 467, 395
Paczynski B., 1983, ApJ, 267, 315
Perego A. et al., 2020, ApJ, 925, 22
Perego A., Rosswog S., Cabezón R. M., Korobkin O., Käppeli R., Arcones A., Liebend"orfer M., 2014, Mon. Not. Roy. Astron. Soc., 443, 3134
Perego A., Radice D., Bernuzzi S., 2017, Astrophys. J. Lett., 850, L37
Perego A., Thielemann F.-K., Cescutti G., 2021, in Bambi C., Katsanevas S., Kokkotas K. D., eds, Handbook of Gravitational Wave Astronomy. Springer, p. 1
Pian E. et al., 2017, Nature, 551, 67
Piro A. L., Kollmeier J. A., 2018, Astrophys. J., 855, 103
Piro A. L., Morozova V. S., 2016, Astrophys. J., 826, 96
Prakash A. et al., 2021, Phys. Rev. D, 104, 083029
Radice D., 2017, Astrophys. J. Lett., 838, L2
Radice D., 2020, Symmetry, 12, 1249
Radice D., Rezzolla L., 2012, Astron. Astrophys., 547, A26
Radice D., Rezzolla L., Galeazzi F., 2014a, Class. Quant. Grav., 31, 075012
Radice D., Rezzolla L., Galeazzi F., 2014b, Mon. Not. Roy. Astron. Soc., 437, L46
Radice D., Rezzolla L., Galeazzi F., 2015, ASP Conf. Ser., 498, 121
Radice D., Galeazzi F., Lippuner J., Roberts L. F., Ott C. D., Rezzolla L., 2016, Mon. Not. Roy. Astron. Soc., 460, 3255
Radice D., Perego A., Hotokezaka K., Fromm S. A., Bernuzzi S., Roberts L. F., 2018, Astrophys. J., 869, 130
Radice D., Bernuzzi S., Perego A., 2020, Ann. Rev. Nucl. Part. Sci., 70, 95
Roberts L. F., Kasen D., Lee W. H., Ramirez-Ruiz E., 2011, Astrophys. J. Lett., 736, L21
Rodrigo C., Solano E., 2020, in XIV.0 Scientific Meeting (virtual) of the Spanish Astronomical Society. p. 182
Rodrigo C., Solano E., Bayo A., 2012, SVO Filter Profile Service Version 1.0. IVOA Working Draft 15 October 2012
Rossi A. et al., 2020, MNRAS, 493, 3379
Rosswog S., Davies M., 2002, MNRAS, 334, 481
Rosswog S., Liebendoerfer M., 2003, MNRAS, 342, 673
Rosswog S., Liebendoerfer M., Thielemann F., Davies M., Benz W., Piran T., 1999, Astron. Astrophys., 341, 499
Rosswog S., Ramirez-Ruiz E., Davies M. B., 2003, MNRAS, 345, 1077
Rosswog S., Piran T., Nakar E., 2013, MNRAS, 430, 2585
Rosswog S., Korobkin O., Arcones A., Thielemann F., Piran T., 2014, MNRAS, 439, 744
Rosswog S., Feindt U., Korobkin O., Wu M. R., Sollerman J., Goobar A., Martinez-Pinedo G., 2017, Class. Quant. Grav., 34, 104001
Rosswog S., Sollerman J., Feindt U., Goobar A., Korobkin O., Wollaeger R., Fremling C., Kasliwal M., 2018, Astron. Astrophys., 615, A132
Roth N., Kasen D., 2015, Astrophys. J. Suppl., 217, 9
Ruffert M., Janka H., Schaefer G., 1996, Astron. Astrophys., 311, 532
Sekiguchi Y., Kiuchi K., Kyutoku K., Shibata M., 2011, Phys. Rev. Lett., 107, 051102
Sekiguchi Y., Kiuchi K., Kyutoku K., Shibata M., 2015, Phys. Rev. D, 91, 064059
Sekiguchi Y., Kiuchi K., Kyutoku K., Shibata M., Taniguchi K., 2016, Phys. Rev. D, 93, 124046
Shibata M., Hotokezaka K., 2019, Ann. Rev. Nucl. Part. Sci., 69, 41
Shibata M., Fujibayashi S., Sekiguchi Y., 2021, Phys. Rev. D, 103, 043022

Siegel D. M., 2019, Eur. Phys. J.A, 55, 203
Siegel D. M., Metzger B. D., 2018, Astrophys. J., 858, 52
Siegel D. M., Ciolfi R., Rezzolla L., 2014, Astrophys. J. Lett., 785, L6
Smartt S. et al., 2017, Nature, 551, 75
Soares-Santos M. et al., 2017, Astrophys. J. Lett., 848, L16
Steiner A. W., Hempel M., Fischer T., 2013, Astrophys. J., 774, 17
Stone J. M., Tomida K., White C. J., Felker K. G., 2020, ApJS, 249, 4
Tanaka M. et al., 2017, Publ. Astron. Soc. Jap., 69, 102
Tanaka M., Hotokezaka K., 2013, Astrophys. J., 775, 113
Tanaka M. et al., 2018, Astrophys. J., 852, 109
Tanaka M., Kato D., Gaigalas G., Kawaguchi K., 2020, MNRAS, 496, 1369
Tanvir N. et al., 2017, Astrophys. J. Lett., 848, L27
Tanvir N., Levan A., Fruchter A., Hjorth J., Wiersema K., Tunnicliffe R., de Ugarte Postigo A., 2013, Nature, 500, 547
Troja E. et al., 2017, Nature, 551, 71
Troja E. et al., 2019, MNRAS, 489, 2104
Typel S., Ropke G., Klahn T., Blaschke D., Wolter H., 2010, Phys. Rev. C, 81, 015803
Villar V. A. et al., 2017, Astrophys. J. Lett., 851, L21
Vincent T., Foucart F., Duez M. D., Haas R., Kidder L. E., Pfeiffer H. P., Scheel M. A., 2020, Phys. Rev. D, 101, 044053
Waxman E., Ofek E. O., Kushnir D., Gal-Yam A., 2018, Mon. Not. Roy. Astron. Soc., 481, 3423
Waxman E., Ofek E. O., Kushnir D., 2019, Astrophys. J., 878, 93
Weiss A., Hillebrandt W., Thomas H.-C., Ritter H., 2004, in Weiss A., Hillebrandt W., Thomas H.-C., Ritter H., eds, Cox and Giuli's Principles of Stellar Structure. Cambridge Scientific Publishers, Cambridge, UK
Wollaeger R. T. et al., 2018, MNRAS, 478, 3298
Wollaeger R. T., van Rossum D. R., Graziani C., Couch S. M., Jordan IV G. C., Lamb D. Q., Moses G. A., 2013, ApJS, 209, 36
Yang B. et al., 2015, Nature Commun., 6, 7323
Zhu Y. L., Lund K. A., Barnes J., Sprouse T. M., Vassh N., McLaughlin G. C., Mumpower M. R., Surman R., 2021a, ApJ, 906, 94
Zhu Y., Lund K., Barnes J., Sprouse T., Vassh N., McLaughlin G., Mumpower M., Surman R., 2021b, Astrophys. J., 906, 94

APPENDIX A: IMPACT OF OPACITY FORMULA

We study the sensitivity of kilonova light curves to the opacity formula mentioned in Section 2.2. We fix the maximum and minimum opacity to 10 cm^2 g^{-1} and 1 cm^2 g^{-1}, respectively, and also fix the intermediate point ($Y_e = 0.25$, $\kappa = 5.5$ cm^2 g^{-1}). We explore the impact of the slope of the transition near $Y_e = 0.25$, which is indicated by parameter s in the following formula:

$$\kappa = 1 + \frac{9}{1 + (4Y_e)^s} \ [\mathrm{cm^2 g^{-1}}]. \quad \text{(A1)}$$

Fig. A1 shows the range of the slope we test, with $s = 12$ being the baseline used in the body of the paper. $s = 24$ results in the sharpest transition, while $s = 4$ produces the mildest transition so that opacity cannot reach its minimum at $Y_e = 0.5$.

Fig. A2 shows the AB magnitudes and the opacity at the luminosity shell for the BLh binary, using $s = 24$, 12, and 4. The definition of luminosity shell is given in Section 4.1. The outermost fast high-Y_e component is not affected by the modification of the opacity formula, producing the first peak of the light curve. For $s = 4$, the effect of lanthanide curtain is alleviated but still present due to the very low Y_e (∼0.15) of the component shown in Fig. 5. As shown by the opacity at luminosity shell, the opacity plateau is only a little smaller than 10 cm^2 g^{-1}, so most of the radiation is trapped inside. At late times, for $s = 4$, the opacity of the inner high-Y_e component increases compared to the baseline. Therefore, it is natural that the radiation is inhibited, and that the kilonova is redder and becomes transparent later. However, these are only minor changes to the light curves, and, in general, the results are not sensitive to the opacity formula.

We do not report the results for the SFHo binary, but the opacity formula also has little impact on SFHo results. The DD2 binary is shown in Fig. A3. For this model, we find that the slope of the opacity profile has essentially no impact. In fact, the outer part of the DD2 profile has a Y_e near 0.25 (Fig. 6), so formulae with different slopes result in similar opacities.

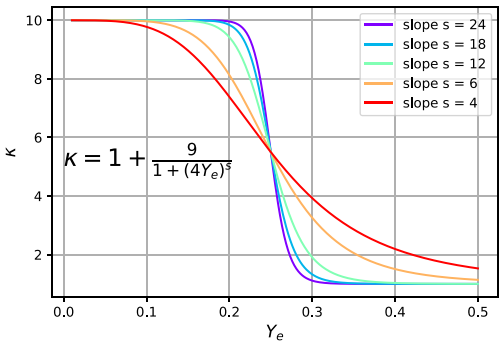

Figure A1. Opacity as a function of initial Y_e. Different from equation (1), the slope of the opacity transition near $Y_e = 0.25$ is a free parameter here, which is indicated by s. s ranges from 4 to 24, and $s = 12$ is the baseline adopted in the main body of the paper.

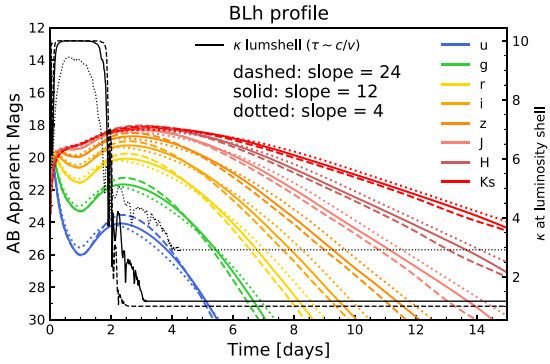

Figure A2. AB magnitudes and the opacity at the luminosity shell for BLh model. Although the magnitudes change a little, the morphology of the light curves remains unchanged in general.

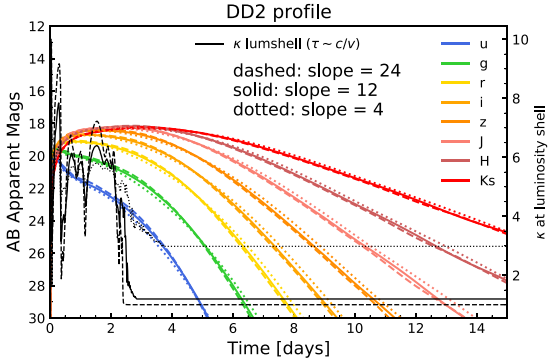

Figure A3. AB magnitudes and the opacity at the luminosity shell for DD2 model. The light curves are insensitive to the slope of the transition in the opacity formula.

APPENDIX B: BOUNDARY VELOCITY

At the outer boundary, the SNEC code sets pressure, temperature, and density to zero. Among them, only the pressure $p_{\rm imax}$ is important since the other quantities are not actually used in the evolution. However, the $p_{\rm imax} = 0$ boundary condition can lead to a large pressure gradient at the boundary when the simulation begins. At that time, the ejecta is very hot ($\sim 10^9$ K) and $p_{\rm imax-1}$ is dominated by the radiation pressure, which is proportional to $T^4_{\rm imax-1}$. This discontinuity causes the velocity near outer boundary to increase to very large values, sometimes even exceeding the speed of light (e.g. BLh profile).

For the wind profiles, one of the solutions is to modify the initial temperature distribution. Instead of using the uniform 10^9 K, we use a power-law decay near the outer boundary, which is already introduced in equation (6). We tested various power-law indexes and found that $\alpha \gtrsim 6$ is enough to solve the problem (Fig. B1).

For realistic profiles, the problem can be alleviated by smoothing the initial velocity distribution. Fig. B2 shows the piecewise fit for BLh profile ($m < m_1$: linear; $m_1 < m < m_2$: exponential; $m > m_2$: polynomial). We call the new profile BLh-with-modified-velocity profile, or BLh–mvel profile. We show light curves produced with this modified profile in Section 4.2. With the BLh–mvel profile, the maximum velocity at the outer boundary is reduced to around 0.8 c (Fig. B3).

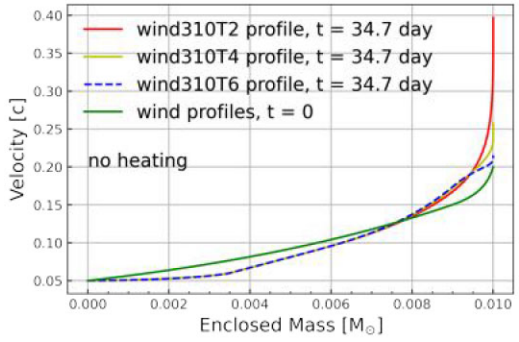

Figure B1. Initial and final velocity as a function of mass for the wind310TX profiles. In this test, r-process heating is turned off to preclude its effects on the velocity. The green line shows the initial velocity distribution, while the other lines show the final velocity distribution using the modified temperature profiles with power-law index = 2, 4, 6, respectively. A power-law factor large enough for temperature effectively reduces the pressure gradients at the outer boundary and thus mitigates the boundary velocity divergence problem.

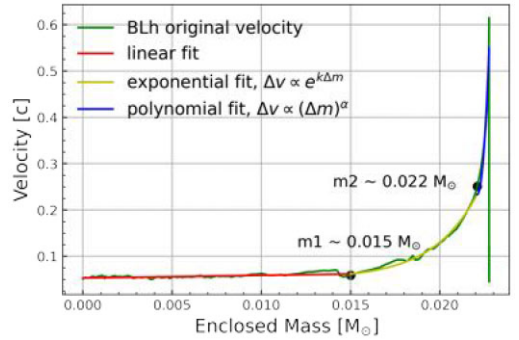

Figure B2. Velocity profile for the BLh and the BLh with modified velocity (BLh–mvel) profiles. We use a piecewise function to fit the initial velocity in BLh profile. We set m_1 and m_2 to 0.015 and 0.022 $M_\odot$, respectively. When $m < m_1$, velocity in BLh–mvel profile grows linearly with m. When m is between m_1 and m_2, $(v - v(m_1))$ is proportional to e^{m-m_1}. When $m > m_2$, we use the function $v - v(m_2) = C(m - m_2)^\alpha$ to fit.

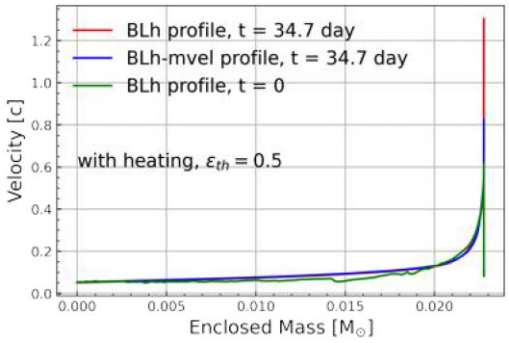

Figure B3. Velocity as a function of mass for the BLh and BLh–mvel profiles. Due to unphysical pressure gradient at the outer boundary and r-process heating, the velocity at the outer boundary can even exceed the speed of light. The problem is less severe for BLh–mvel than for BLh profile. Since the mass and energy near outer boundary accounts only for a very small part of the whole ejecta, we find that it does not affect light curves.

The above changes to the initial profiles indicate that the boundary velocity problem is profile-dependent. However, the final light curves are largely unaffected by these dynamics close to the outer boundary. This is because the region affected by the outer boundary encloses a small amount of material, as shown in Fig. B3. The increase of the kinetic energy due to the boundary velocity problem is not large enough to visibly affect the light curves, as can be observed by comparing the light curves obtained with the BLh and the BLh–mvel profiles shown in Fig. 16.

APPENDIX C: METHOD OF BLH EXTRAPOLATION

We extrapolate the BLh profile by fitting all thermodynamic quantities in time and then extrapolating them. Specifically, we integrate the outflow rate from the WhiskyTHC simulations to obtain the mass of the material that has crossed an extraction sphere with $r = 295$ km as a function of time. We denote the mass of the ejecta still enclosed by $r = 295$ km at time t as $m(t)$. The mass of the material that has crossed the extraction sphere at any given time is as $M_{\rm tot} - m(t)$. We

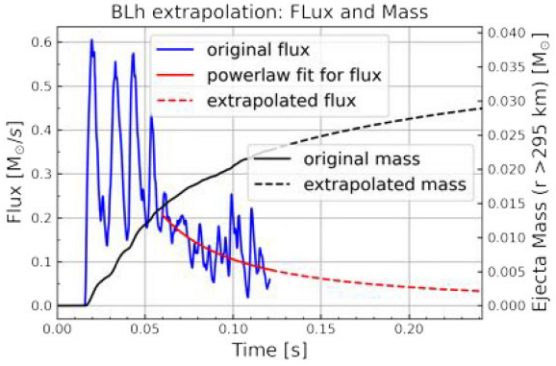

Figure C1. Mass extrapolation for the BLh profile. We use a power law to fit ejecta flux after 0.06 s and then extrapolate it to $t_{\rm end}$. From the integration of the flux at 295 km, we obtain the mass of ejecta outside 295 km as a function of time (black lines, solid: original data; dashed: extrapolated).

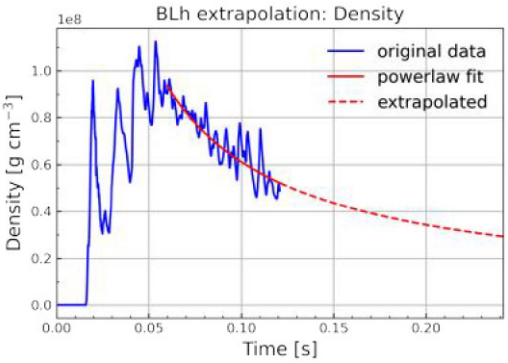

Figure C2. Density extrapolation for the BLh profile. We first reconstruct the density at 295 km as a function of time according to the BLh profile and its mass flux at 295 km (blue line). Then, we use a power law to fit the density after 0.06 s (red solid line). Finally, we extrapolate the power law to $t_{\rm end}$ (red dashed line), e.g. 0.24 s in the figure.

use a power law to fit the mass flux after 0.06 s and then extrapolate it to $t_{\rm end}$. Fig. C1 shows the case in which $t_{\rm end} = 0.24$ s, that is twice the original simulation time for the BLh binary. Note that here the time is given from the beginning of `WhiskyTHC` simulations and includes the period before the merger. With the extrapolation, the total ejecta mass increases from 0.022 $M_\odot$ to 0.029 $M_\odot$.

For each profile, we have density, velocity, temperature, etc., as a function of enclosed mass. For instance, the density profile is $\rho(m)$. Since we know the function $m(t)$, we can use it to calculate the time at which each Lagrangian fluid element crosses the extraction sphere. From this, we can obtain $\rho(t)$ on the extraction sphere. We fit $\rho(t)$ after 0.06 s with a power law and extrapolate it to $t_{\rm end}$ (see Fig. C2). As a last step, we convert the extrapolated $\rho(t)$ back to $\rho(m)$ and get the new profile.

This extrapolation methodology is not necessarily limited to power-law extrapolation. Indeed, we use power-law fits for the mass flux and the density, a linear function for the entropy, and a constant for temperature, velocity, initial $Y_{\rm e}$, and expansion time-scale.

APPENDIX D: ENERGY CONSERVATION FOR BLH PROFILE

We check energy conservation for the optimal wind profiles in Section 3.1. Here, we repeat this analysis for the BLh profile. Other simulation profiles behave in a similar way. As shown in Fig. D1, the total energy is initially negative, because the profile is initially still gravitationally bound. However, the mechanical work done on the inner boundary by pressure forces and r-process heating unbinds the ejecta. This is expected, since we use the Bernoulli criterion to identify the ejecta in the merger simulations (e.g. Kastaun & Galeazzi 2015). After this initial phase that lasts about 1 s, the total energy of the ejecta is dominated by the kinetic energy (see Fig. D2), as was the case for the wind profiles. When the total energy crosses zero, there is a jump in the relative difference between E1 (the total energy of the ejecta) and E2 (initial ejecta energy + r-process heating + pdV work − radiated energy). After 0.14 s, the relative difference between E1 and E2 drops to below 0.2 per cent. We conclude that `SNEC` conserves energy very well with the adopted setup.

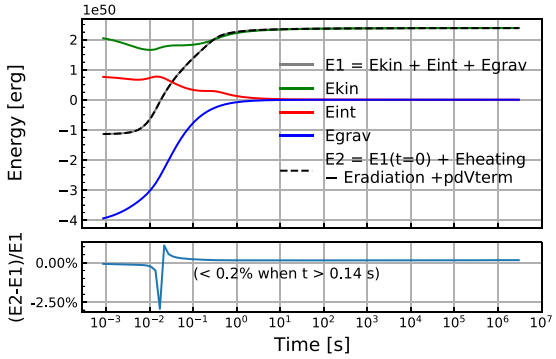

Figure D1. Same as Fig. 7 but for the BLh profile. The total energy is negative initially due to large gravitational energy but soon becomes positive as a result of the mechanical work done on the inner boundary. The large spike in the relative difference between E1 and E2 is caused by total energy changing sign. The difference drops to below 0.2 per cent after 0.14 s, so energy is well conserved.

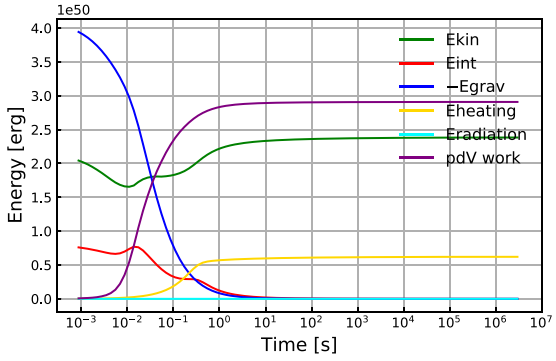

Figure D2. Different energy terms as a function of time for the BLh model. The total energy is at first dominated by gravitational energy. pdV work at inner boundary and the r-process heating increase the total energy of the ejecta from negative to positive. Afterwards, the total energy is dominated by kinetic energy, like for the wind profiles. Only a small fraction of the energy is radiated as most of the specific internal energy is lost to expansion.

This paper has been typeset from a TEX/LATEX file prepared by the author.